

Photospheric processes and magnetic flux tubes

Oskar Steiner

Kiepenheuer Institut für Sonnenphysik, Schöneckstrasse 6, D-79104, Freiburg, Germany

Abstract. New high-resolution observations reveal that small-scale magnetic flux concentrations have a delicate substructure on a spatial scale of $0.1''$. Their basic structure can be interpreted in terms of a magnetic flux sheet or tube that vertically extends through the ambient weak-field or field-free atmosphere with which it is in mechanical equilibrium. A more refined interpretation comes from new three-dimensional magnetohydrodynamic simulations that are capable of reproducing the corrugated shape of magnetic flux concentrations and their signature in the visible continuum. Faculae are another manifestation of small-scale magnetic flux concentrations. It is shown that the characteristic asymmetric shape of the contrast profile of faculae is an effect of radiative transfer across the rarefied atmosphere of the magnetic flux concentration. Also discussed are three-dimensional radiation magnetohydrodynamic simulations of the integral layers from the top of the convection zone to the mid-chromosphere. They show a highly dynamic chromospheric magnetic field, marked by rapidly moving filaments of stronger than average magnetic field that form in the compression zone downstream and along propagating shock fronts. The simulations confirm the picture of flux concentrations that strongly expand through the photosphere into a more homogeneous, space filling chromospheric field. Future directions in the simulation of small-scale magnetic fields are indicated with a few examples from recent reports.

The second part of these lecture notes is devoted to a few basic properties of magnetic flux tubes that can be considered to be an abstraction of the more complicated flux concentrations known from observations and numerical simulations. By analytical means we will find that an electrical current flows in a sheet at the surface of a flux-tube for which location we also derive the mechanical equilibrium condition. The equations for constructing a magnetohydrostatic flux tube embedded in a gravitationally stratified atmosphere are derived. It is shown that the expansion of a flux tube with height sensibly depends on the difference in the thermal structure between the atmosphere of the flux tube and the surrounding atmosphere. Furthermore, we will find that radiative equilibrium produces a smaller temperature gradient within the flux tube compared to that in the surrounding atmosphere. The condition for interchange stability is derived and it is shown that small-scale magnetic flux concentrations are liable to the interchange instability.

Keywords: Sun – magnetic fields – photosphere – chromosphere

PACS: 96.60.Mz

PART I: THE SIMULATION OF SMALL-SCALE MAGNETIC FIELDS

With “realistic simulations” computational physicists aim at imitating real physical processes that occur in nature. In the course of rebuilding nature in the computer, they aspire to a deeper understanding of the process under investigation. In some sense the opposite approach is taken by computational physicists that aim at separating the fundamental physical processes by abstraction from the particulars for obtaining “ideal simulations” or an analytical model of the essential physical process. Both strategies are needed and are complementary. In the first part of these lecture notes, we mainly focus on “realistic simulations” and comparison with observations and provide a more abstract

background in the second part.

The term small-scale flux concentration is used here to designate the magnetic field that appears in G-band filtergrams as bright tiny objects within and at vortices of intergranular lanes. They are also visible in the continuum, where they are called *facular points* [1], while the structure made up of bright elements is known as the *filigree* [2]. In more recent times, the small-scale magnetic field was mostly observed in the G band (a technique originally introduced by Muller [3]) because the molecular band-head of CH that constitutes the G band acts as a leverage for the intensity contrast [4, 5, 6, 7, 8]. Being located in the blue part of the visible spectrum, this choice also helps improving the diffraction limited spatial resolution and the contrast in the continuum.

Small-scale magnetic flux concentrations are studied for several reasons:

- Since they make up the small end of a hierarchy of magnetic structures on the solar surface, the question arises whether they are “elemental” or whether yet smaller flux elements exist. How do they form? Are they a surface phenomenon? What is their origin?
- Near the solar limb they can be identified with faculae, known to critically contribute to the solar irradiance variation.
- They probably play a vital role in the transport of mechanical energy to the outer atmosphere, e.g., by guiding and converting magnetoacoustic waves generated by the convective motion and granular buffeting or, more directly, by ohmic dissipation.

STRUCTURE OF SMALL-SCALE MAGNETIC FLUX CONCENTRATIONS

Recent observations of unprecedented spatial resolution with the 1 m Swedish Solar Telescope by [9] and [10] reveal G-band brightenings in an active region as delicate, corrugated ribbons that show structure down to the resolution capability of the instrument of $0.1''$, while isolated point-like brightenings exist as well. The structure made up of these objects evolves on a shorter than granular time-scale, giving the impression of a separate (magnetic) fluid that resists mixing with the granular material. Figure 1 shows an example G-band filtergram from the former paper taken in a remnant active region plage near disk center. In this region, intergranular lanes are often completely filled with magnetic field like in the case marked by the white, horizontal lines in Fig. 1. There, and in other similar cases, the magnetic field concentration is framed by a striation of bright material, while the central part is dark. Besides examples of ribbon bands, Figure 1 shows also an isolated bright point in the lower right corner.

The graphic to the right hand side of Fig. 1 displays the emergent G-band intensity (solid curve) from the cross section marked by the white horizontal lines in the image to the left. Also shown are the corresponding magnetographic signal (dashed curve), the blue continuum intensity (dotted), and the Ca H-line intensity (dash-dotted). We note that the magnetic signal is confined to the gap between the two horizontal white lines. The intensities show a two-humped profile.

This situation reminds of the flux-sheet model and the “bright wall effect” of earlier theoretical work. A first quasi-stationary, self-consistent simulation of a small-scale flux

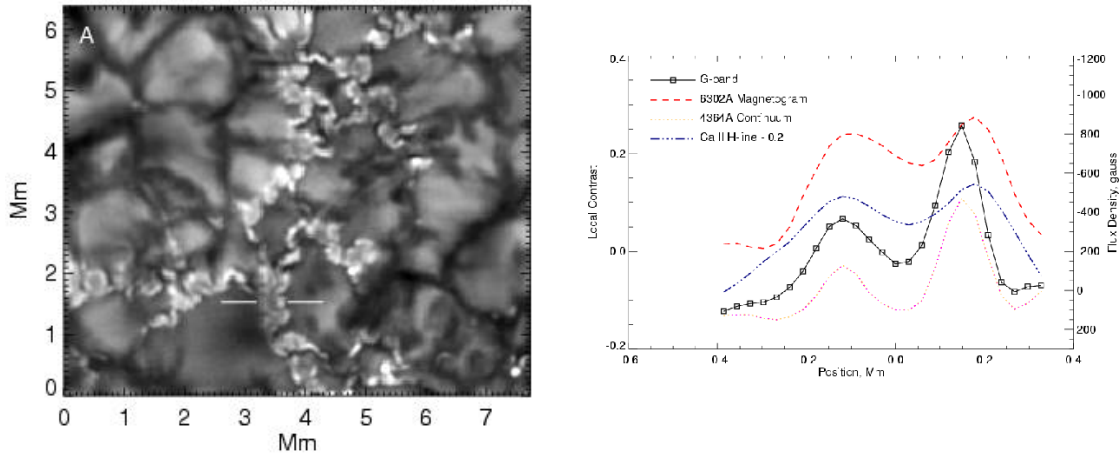


FIGURE 1. *Left:* G-band filtergram showing the ribbon-like shape of magnetic flux concentrations. *Right:* G-band intensity (solid curve) along the section indicated by the horizontal white lines in the image to the left. Also shown are the magnetogram signal, the continuum intensity at 436.4 nm, and the Ca II H-line intensity down-shifted by 0.2. From Berger et al. [9].

sheet was carried out by Deinzer et al. [11, 12], popularly known as the “KGB-models”. The basic properties of this model are sketched in Fig. 2. (A first kind of this sketch was published by Zwaan [13].) Accordingly, a small-scale flux concentration, either of tube or sheet-like shape, is in mechanical equilibrium with the ambient atmosphere, viz., the gas plus magnetic pressure of the atmosphere within the tube/sheet balances the gas pressure in the ambient (field-free) medium. This calls for a reduced density in the flux concentration with respect to the environment, at least in the photospheric part, where the radiative heat exchange quickly drives the configuration towards radiative equilibrium, hence to a similar temperature at constant geometrical height. The density reduction renders the flux tube/sheet atmosphere more transparent, which causes a depression of the surface of constant optical depth, as indicated by the surface of $\tau_c = 1$ in Fig. 2. In a plage or network region, this effect increases the “roughness” of the solar surface, hence the effective surface from which radiation can escape, which increases the net radiative loss from these areas.

The graphics to the right hand side of Fig. 2 shows a sketch of the relative intensity emerging from this model, viz., the intensity of light propagating in the vertical direction as a function of distance from the flux sheet’s plane of symmetry. It corresponds to the plot on the right hand side of Fig. 1. The similarity between this model and the observation is striking. Turning to a narrower flux sheet/tube would result in the merging of the two contrast peaks to a single central peak in both, model and observation, i.e., to a ribbon band or bright point, respectively. Yet, the striation of the depression wall that can be seen in the observation is of course not reproduced by the model, which is strictly two-dimensional with translational invariance in lane direction. We will see in the section on the physics of faculae that three-dimensional magnetoconvection simulations show a rudimentary striation. The physical origin of the striation is still unknown.

Accordingly, the basic properties of ribbon-like magnetic flux concentrations can be understood in terms of a magnetic flux sheet embedded in and in force balance with a

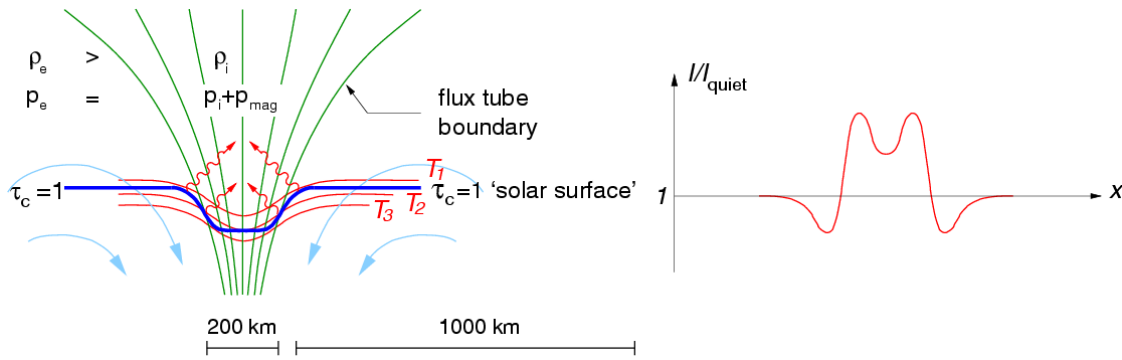


FIGURE 2. Sketch of a magnetic flux sheet (left) with corresponding intensity contrast (right), distilled from self-consistent numerical MHD simulations. Note that the isothermal surfaces are not exactly parallel to the surface of optical depth unity, which gives rise to the particular M-shape of the contrast profile. From Steiner [14].

more or less field-free ambient medium. This can also be said (replacing the word sheet by tube) of the rosette structure visible in other still images of Berger et al. [9] who call it “flower-like”. Flowers can transmute to pores and vice versa. The striation of their bright collar is similar to that seen in ribbon structures. Discarding the striation, the basic properties of flowers can well be interpreted in terms of a tube shaped flux concentration like the one sketched in Fig. 2 or shown in Fig. 30.

A 2 h sequence of images by Rouppe van der Voort et al. [10] with a quality comparable to Fig. 1 reveals that the shape of the ribbon-like flux concentrations and the striation of ribbons and flowers change on a very short time-scale, of the order of the Alfvén crossing travel time. This suggests that these morphological changes and the striation itself are related to the flute instability, which small-scale flux concentrations are liable to. For an untwisted axisymmetric flux tube, the radial component of the magnetic field at the flux-tube surface must decrease with height, $dB_r/dz|_S < 0$, in order that the flux tube is stable against the flute (interchange) instability [15]. While sunspots and pores with a magnetic flux in excess of $\Phi \approx 10^{11}$ Wb do meet this condition, small-scale flux concentrations do not fulfill it [16, 17, 18]. Bünte [19] shows that small-scale flux sheets too, are flute unstable, and he concludes that filament formation due to the flute instability close to the surface of optical depth unity would ensue. As the flux sheet is bound to fall apart because of the flute instability, its debris are again reassembled by the continuous advection of strands of magnetic field back to the intergranular lane so that a competition between the two effects is expected to take place, which might be at the origin of the corrugation of the field concentrations and of the striation of the tube/sheet interface with the ambient medium. For a derivation of the flute-instability condition see part II of these lecture notes.

Although the fine structure of small-scale magnetic flux concentrations changes on a very short time scale, single flux elements seem to persist over the full duration of the time sequence of 2 h. They may dissolve or disappear for a short period of time, but it seems that the same magnetic flux continually reassembles to make them reappear nearby. Latest G-band time sequences obtained with the Solar Optical Telescope (SOT) on board of the Japanese space satellite HINODE

(<http://solarb.msfc.nasa.gov>) confirm these findings even for G-band bright points of low intensity. This suggest a deep anchoring of at least some of the flux elements although numerical simulation seem not to confirm this conjecture.

As indicated in the sketch of Fig. 2, the magnetic flux concentration is framed by a downflow of material, fed by a horizontal flow that impinges on the flux concentration. Already the flux-sheet model of Deinzer et al. [12] showed a persistent flow of this kind. According to these authors it is due to radiative cooling from the depression walls of the magnetic flux concentrations (the “hot wall effect”) that causes a horizontal pressure gradient, which drives the flow. The non-stationary flux-sheet simulations of Steiner et al. [20] and Leka and Steiner [21] showed a similar persistent downflow, which becomes faster and narrower , with increasing depth, turning into veritable *downflow jets* beneath the visible surface. While downflows in the periphery of pores have been observed earlier [21, 22, 23] and also horizontal motions towards a pore [24], only very recently such an accelerating downflow has been observationally detected in the immediate vicinity of ribbon bands by Langanen et al. [25].

SIMULATION OF SMALL-SCALE MAGNETIC FLUX CONCENTRATIONS

For a realistic simulation of small-scale magnetic flux concentrations in the solar photosphere one must solve the system of the magnetohydrodynamic equations including continuum, momentum, induction, and energy equation, preferably in three spatial dimensions. Since flux concentrations are predominantly governed by convective motion, at least the surface layers of the convection zone must be taken into account in order to obtain reliable results for the magnetic field in the photosphere. Hence, the computational domain must span the distinct radial section of the sun, where energy transport changes from convective to radiative so that radiative transfer must be taken into account in the energy equation. An equation of state and opacities appropriate for the solar plasma in the region of interest are essential for a realistic simulation. The spatial extent of the computational domain is limited by the computational resources and the minimally required spatial resolution. Since we would like to resolve at least magnetic flux concentrations with a size of 100 km we should have a grid constant not surpassing about 10 km in the horizontal direction. In the vertical direction the resolution can be adjusted according to the variation of the pressure scale height but should also be at least ≈ 10 km in the photosphere. Considering that a computational grid with 1000^3 grid cells is definitely the uppermost limit for present day simulations, we obtain a size limit for the computational domain of about $(10 \text{ Mm})^3$.

Fig. 3 shows the typical size of the horizontal extent of a two-dimensional and a three-dimensional computational domain as used in the past, in relation to granulation and G-band bright points. We should be aware that such a computational box, despite the large number of grid cells, encompasses a tiny portion, only, of the solar convection zone. This is illustrated in Fig. 4, where the computational box of the size given to the left, is shown in relation to the size of the solar convection zone. Yet, this tiny computational box includes the full height range of the photosphere and the mass density varies by about a factor of 10^5 . Even though the box reaches only 1.4 Mm into the convection

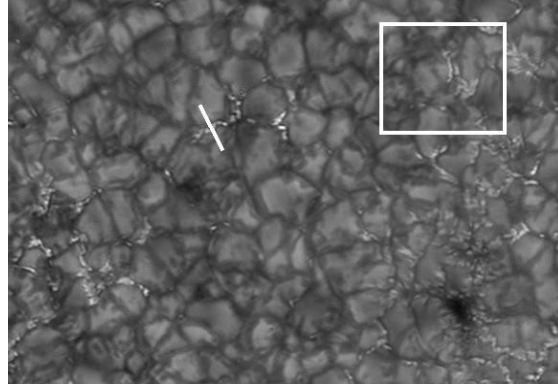


FIGURE 3. G-band filtergram of an area of 32×22 arcs of the solar surface. The white line drawn across an elongated bright ribbon band corresponds to the width of a two-dimensional simulation domain of 2400 km. The white box shows the size of a three-dimensional simulation domain of 4800×4800 km. Image by K. Mikurda, F. Wöger, & O. von der Lühse with the Vacuum Tower Telescope (VTT) at Tenerife.

zone, it probes a depth range of already about 5 pressure scale heights of the convective layers and hydrogen changes from completely neutral to a substantial fraction being ionized.

The ideal MHD-equations can be written in conservative form as:

$$\frac{\partial \mathbf{U}}{\partial t} + \nabla \cdot \mathcal{F} = \mathbf{S}, \quad (1)$$

where the vector of conserved variables, \mathbf{U} , the source vector, \mathbf{S} , due to gravity and radiation, and the flux tensor, \mathcal{F} , are

$$\mathbf{U} = (\rho, \rho \mathbf{v}, \mathbf{B}, E), \quad \mathbf{S} = (0, \rho \mathbf{g}, 0, \rho \mathbf{g} \cdot \mathbf{v} + q_{\text{rad}}), \quad (2)$$

$$\mathcal{F} = \begin{pmatrix} \rho \mathbf{v} \\ \rho \mathbf{v} \mathbf{v} + \left(p + \frac{\mathbf{B} \cdot \mathbf{B}}{2\mu} \right) \mathbf{I} - \frac{\mathbf{B} \mathbf{B}}{\mu} \\ \mathbf{B} \mathbf{v} - \mathbf{v} \mathbf{B} \\ \left(E + p + \frac{\mathbf{B} \cdot \mathbf{B}}{2\mu} \right) \mathbf{v} - \frac{1}{\mu} (\mathbf{v} \cdot \mathbf{B}) \mathbf{B} \end{pmatrix}, \quad (3)$$

and where the dyadic tensor product of two vectors \mathbf{a} and \mathbf{b} is the tensor $\mathbf{ab} = \mathbf{C}$ with elements $c_{mn} = a_m b_n$. \mathbf{v} and \mathbf{B} are vectors of the velocity and magnetic fields. μ is the magnetic permeability, which can be taken to be $\mu = \mu_0 = 4\pi \cdot 10^{-7} [\text{V s A}^{-1} \text{m}^{-1}]$ for the solar plasma. \mathbf{I} is the identity matrix and $\mathbf{a} \cdot \mathbf{b} = \sum_k a_k b_k$ the scalar product of the two vectors \mathbf{a} and \mathbf{b} .

The total energy E is given by

$$E = \rho \varepsilon + \rho \frac{\mathbf{v} \cdot \mathbf{v}}{2} + \frac{\mathbf{B} \cdot \mathbf{B}}{2\mu}, \quad (4)$$

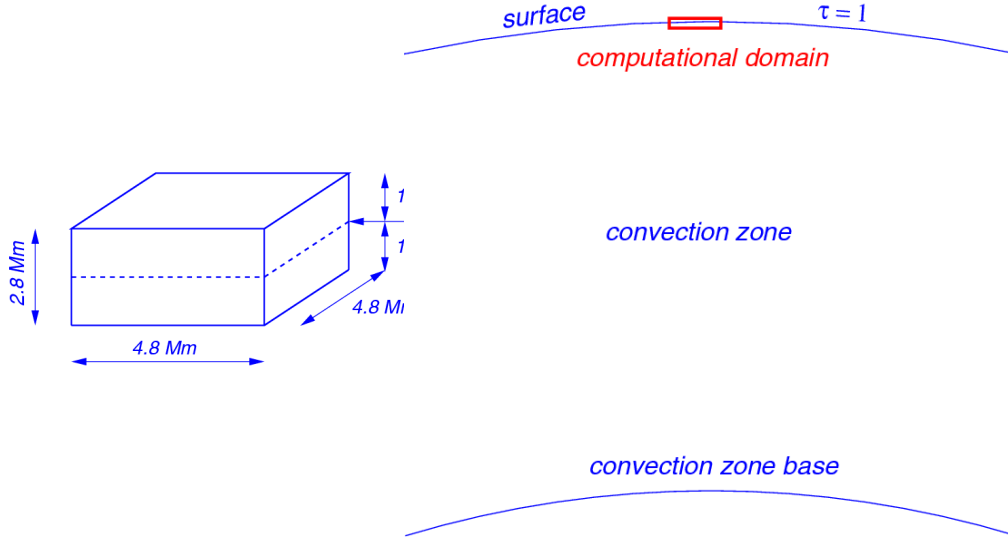


FIGURE 4. Typical size of a three-dimensional computational box (left) on scale with the convection zone boundaries of the sun (right).

where ε is the thermal energy per unit mass. The additional solenoidality constraint,

$$\nabla \cdot \mathbf{B} = 0, \quad (5)$$

must also be fulfilled. The MHD equations must be closed by an equation of state which gives the gas pressure, p , as a function of the density and the thermal energy per unit mass

$$p = p(\rho, \varepsilon), \quad (6)$$

usually available to the program in tabulated form.

The radiative source term is given by

$$q_{\text{rad}} = 4\pi\rho \int \kappa_{\nu}(J_{\nu} - B_{\nu})d\nu, \quad (7)$$

where J_{ν} is the mean intensity and B_{ν} the Planck function. Assuming strict local thermodynamic equilibrium (LTE), the intensity is given by the formal solution of the radiative transfer equation:

$$J_{\nu}(\mathbf{r}) = \frac{1}{4\pi} \oint I_{\nu}(\mathbf{r}, \mathbf{n})d\Omega, \quad I_{\nu}(\mathbf{r}, \mathbf{n}) = I_{\nu 0}e^{-\tau_{\nu 0}} + \int_0^{\tau_{\nu 0}} B_{\nu}(\tau_{\nu})e^{-\tau_{\nu}}d\tau_{\nu}, \quad (8)$$

where $\tau_{\nu 0}$ is the optical depth at frequency ν from the boundary to the location \mathbf{r} along the direction \mathbf{n} . $d\tau = \kappa ds$, where κ is the total opacity and s the spatial distance along a line through location \mathbf{r} in direction \mathbf{n} . Formally, this can be written more compact as

$$J_{\nu}(\mathbf{r}) = \Lambda_{\nu}(\mathbf{r}, \mathbf{r}')B_{\nu}(\mathbf{r}') + G_{\nu}(\mathbf{r}), \quad (9)$$

where Λ_{ν} is the integral operator which adds the intensities at \mathbf{r} caused by emission at all the points \mathbf{r}' in the considered computational domain, and where G_{ν} is the transmitted

mean intensity due to the incident radiation field into this domain. In practice the frequency integration is either replaced by using frequency mean quantities (Rosseland mean opacity) or it is approximated by a method of multiple frequency bands [26]. For a detailed description of the latter method see [27] and [28].

In practice it is not the ideal MHD-equations that are solved but rather some kind of a viscous and resistive form of the equations with flux tensor

$$\mathcal{F} = \begin{pmatrix} \rho \mathbf{v} \\ \rho \mathbf{v} \mathbf{v} + \left(p + \frac{\mathbf{B} \cdot \mathbf{B}}{2\mu} \right) \mathbf{I} - \frac{\mathbf{B} \mathbf{B}}{\mu} - \mathbf{R} \\ \mathbf{B} \mathbf{v} - \mathbf{v} \mathbf{B} + \eta [\nabla \mathbf{B} - (\nabla \mathbf{B})^T] \\ \left(E + p + \frac{\mathbf{B} \cdot \mathbf{B}}{2\mu} \right) \mathbf{v} - \frac{1}{\mu} (\mathbf{v} \cdot \mathbf{B}) \mathbf{B} + \eta (\mathbf{j} \times \mathbf{B}) - \mathbf{R} \cdot \mathbf{v} + \mathbf{q}^{\text{turb}} \end{pmatrix}, \quad (10)$$

where $\mathbf{R} = \nu \rho [(\nabla \mathbf{v}) + (\nabla \mathbf{v})^T - (2/3)(\nabla \cdot \mathbf{v})\mathbf{I}]$ is the viscous stress tensor, $\eta = (\nu/\text{Pr}_m) = 1/(\mu\sigma)$ the magnetic diffusivity with σ being the electric conductivity, and $\eta(\mathbf{j} \times \mathbf{B}) = (\eta/\mu)(\nabla \times \mathbf{B}) \times \mathbf{B}$. $\mathbf{R} \cdot \mathbf{v}$ is the tensor product $r_{mk}v_k$. Pr_m is the magnetic Prandtl number. \mathbf{q}^{turb} is a turbulent diffusive heat flux, which would typically be proportional to the entropy gradient: $\mathbf{q}^{\text{turb}} = -(1/\text{Pr})\nu\rho T\nabla s$, where Pr is the Prandtl number.

Typically, ν is not taken to be the molecular viscosity coefficient but rather some *turbulent* value that takes care of the dissipative processes that cannot be resolved by the computational grid. Such *subgrid-scale viscosities* should only act where strong velocity gradients lead to turbulence. Therefore, they typically depend on velocity gradients like in the Smagorinsky-type of turbulent viscosity where

$$\nu^t = c \left\{ 2 \left[\left(\frac{\partial v_x}{\partial x} \right)^2 + \left(\frac{\partial v_y}{\partial y} \right)^2 + \left(\frac{\partial v_z}{\partial z} \right)^2 \right] + \left(\frac{\partial v_x}{\partial y} + \frac{\partial v_y}{\partial x} \right)^2 + \left(\frac{\partial v_x}{\partial z} + \frac{\partial v_z}{\partial x} \right)^2 + \left(\frac{\partial v_y}{\partial z} + \frac{\partial v_z}{\partial y} \right)^2 \right\}^{1/2}, \quad (11)$$

and where c is a free parameter. This parameter is normally chosen as small as possible just in order to keep the numerical integration stable and smooth, but otherwise having no effect on large scales.

Advanced numerical (high resolution) schemes feature an inherent “dissipation” (limiters) that acts similar to the explicit dissipative terms shown in the above flux tensor, Eq. (10). This *artificial viscosity* is made as small as possible but just large enough in order to keep the numerical scheme stable and keep gas pressure and total energy positive. One then only has to program the ideal equations. Of course, in this case it is difficult to quote the actual Reynolds and Prandtl number of the simulation because these numbers change then from grid cell to grid cell depending on the flow. Therefore, for some applications, it might be preferable to explicitly include the dissipative terms in the equations using constant dissipation coefficients, which then allows for well defined dimensionless numbers. However one integrates the ideal equations on a discrete computational grid,

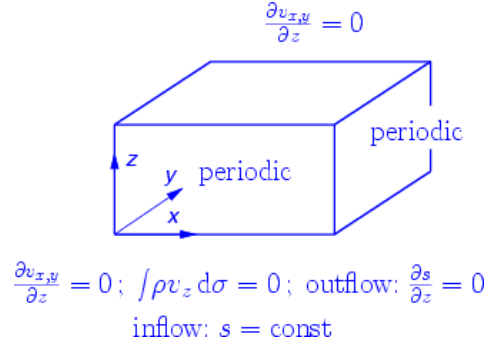


FIGURE 5. Typical boundary conditions for thermal variables and velocities.

one is locked with a discretization error that normally assumes a form similar to the dissipative terms in the non-ideal equations. More details on computational methods for astrophysical fluid flow can be found in LeVeque [29]. Other very useful text books on the numerical solution of the gasdynamics equations are [30, 31, 32]. For corresponding solution methods of the MHD equations see, e.g., [33, 34, 35, 36, 37, 38] and references therein.

Fig. 5 displays typical boundary conditions for thermal variables and velocity. Noteworthy are the conditions at the bottom boundary, where the plasma should freely flow in and out of the computational domain (subject to the constraint of mass conservation) since this boundary is located within the convection zone. Inflowing material has a given specific entropy that determines the effective temperature of the radiation leaving the domain at the top, while the outflowing material carries the entropy it instantly has. This boundary condition reflects that inflowing material originates from the deep convection zone with a close to adiabatic stratification of a fixed entropy.

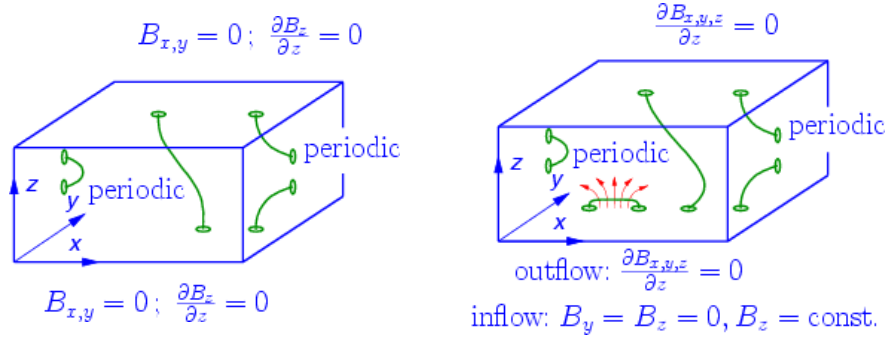


FIGURE 6. Two different realizations for the boundary conditions of the magnetic field. The condition of the right hand panel allows for the transport of horizontal magnetic field of a given strength into the box.

Fig. 6 displays two different realizations (both presently in use) for the boundary conditions of the magnetic field. While the magnetic field in the condition of the left panel is forced to become vertical at the top and bottom boundary, the condition of the right hand panel allows for the transport of horizontal magnetic field of a given strength into the box. More details about this condition are given in the chapter on future directions.

Results from multidimensional simulations

New results from realistic three-dimensional simulations on the formation, dynamics and structure of small-scale magnetic flux concentrations have recently been published in a series of papers by Schüssler and collaborators. Vögler et al. [39] simulate magnetoconvection in a box encompassing an area on the solar surface of $6 \times 6 \text{ Mm}^2$ with a height extension of 1400 km, reaching from the temperature minimum to 800 km below the surface of optical depth unity. Although this is only 0.4% of the convection zone depth, the box still includes the entire transition from almost completely convective to mainly radiative energy transfer and the transition from the regime where the flux concentration is dominated by the convective plasma flow to layers where the magnetic energy density of the flux concentrations by far surpasses the thermal energy density. The bottom boundary in this and similar simulations is open in the sense that plasma can freely flow in and out of the computational domain, subject to the condition of mass conservation. Inflowing material has a given specific entropy that determines the effective temperature of the radiation leaving the domain at the top, while the outflowing material carries the entropy it instantly has.

Figure 7 shows a snapshot from this simulation: To the left the emergent mean intensity, to the right the vertical magnetic field strength at a constant height, viz., at the horizontally averaged geometrical height of optical depth unity. (I would like to caution that this magnetic map is not what would be seen with a magnetograph, irrespective of its spatial resolution, because it refers to a plane parallel section, which is not what is sampled with a magnetographic or polarimetric mapping.) The strong magnetic field in intergranular lanes is manifest in a corresponding signal in the emergent intensity very much like the observations shown in the previous sections (Figs. 1 and 3). Also, the intensity signal shows the same corrugated and knotted ribbon structure that is observed, and sometimes there appear also broader ribbon structures with a dark central core, like the one marked in Fig. 1. The characteristic striation of the latter case however, is absent in the simulation, possibly because the flute instability is suppressed on very small spatial scales due to lack of sufficient resolution of the simulation. In the central part of the snapshot, a micro pore or magnetic knot has formed.

A comparison of the average gas plus magnetic pressure as a function of height at locations of magnetic flux concentrations with the run of the average gas pressure in weak-field regions reveals that the two are almost identical, proving that even in this dynamic regime, the thin flux tube approximation is very well satisfied [39]. This result confirms that the model discussed in the previous section and sketched in Fig. 2 is indeed an acceptable first approximation to the real situation.

Simulations are not just carried out for the sake of reproducing observed quantities. Once good agreement with all kind of observations exists, simulations allow with some confidence to inform about regions not directly accessible to observations, for example about the magnetic structure in subsurface layers. In this respect the simulations of Vögler et al. [39] show that often flux concentrations that have formed at the surface disperse again in shallow depths. This behaviour was also found by Schaffenberger et al. [41] in their simulation with an entirely different code and further by Stein and Nordlund [42]. A vertical section through a three-dimensional simulation domain of Schaffenberger et al. [41], where two such shallow flux concentrations have formed, is

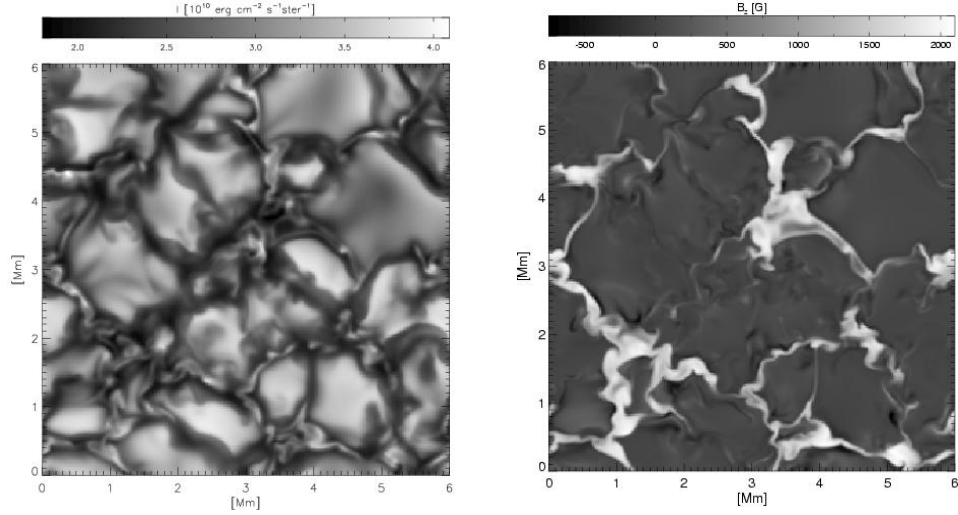


FIGURE 7. Simulation snapshot. *Left:* Frequency integrated intensity. *Right:* Vertical magnetic flux density at constant average geometrical height of optical depth unity. The mean flux density is 0.02 T. From Vögler et al. [39].

shown in Fig. 14. The superficial nature of magnetic flux concentrations in the simulations, however, is difficult to reconcile with the observation that many flux elements seem to persist over a long time period.

Although the turbulent nature of convection requires simulation in three-dimensional space, it can be instructive to carry out less costly two-dimensional calculations that allow for high spatial resolution. For example, a two-dimensional approach can be justified for the simulation of elongated sheets of magnetic flux concentrations as they can be found in intergranular lanes of active regions, e.g., the G-band bright string that extends perpendicular to the 2-D domain indicated in Fig. 3.

Fig. 8 (top) shows a time instant of a two-dimensional simulation of a magnetic flux sheet in interaction with convective motion [20]. A granule has grown to the right of the flux sheet and pushes it to the left. Such “granular buffeting” can produce waves propagating along, within, and in the environment of a magnetic flux sheet. Besides a swaying motion of the flux sheet that excites transverse tube waves, the simulation also revealed that often shock waves propagate in the vertical direction in the tenuous upper photospheric part within the flux sheet. Such a shock wave is visible in Fig. 8 (top) in a height range between 300 to 400 km slightly left of the central part of the flux sheet.

From simulations as the ones shown in Figs. 7 or 8 (top), synthetic observable quantities like intensity contrasts, or spectral lines, or polarimetric quantities can be computed and directly compared with real observations. For example, Fig. 8 (bottom) displays Stokes V profiles computed for vertical lines of sight distributed over the horizontal interval between 600 and 1380 km of the simulation snapshot. The shock wave produces the pathological Stokes V profiles belonging to $x = 900$ and 920 km. There is a systematic change in the area asymmetry of the Stokes V profiles across the flux sheet. While the central part of the flux sheet produces profiles with a negative area asymmetry, the peripheral profiles are positive. This behaviour can be understood,

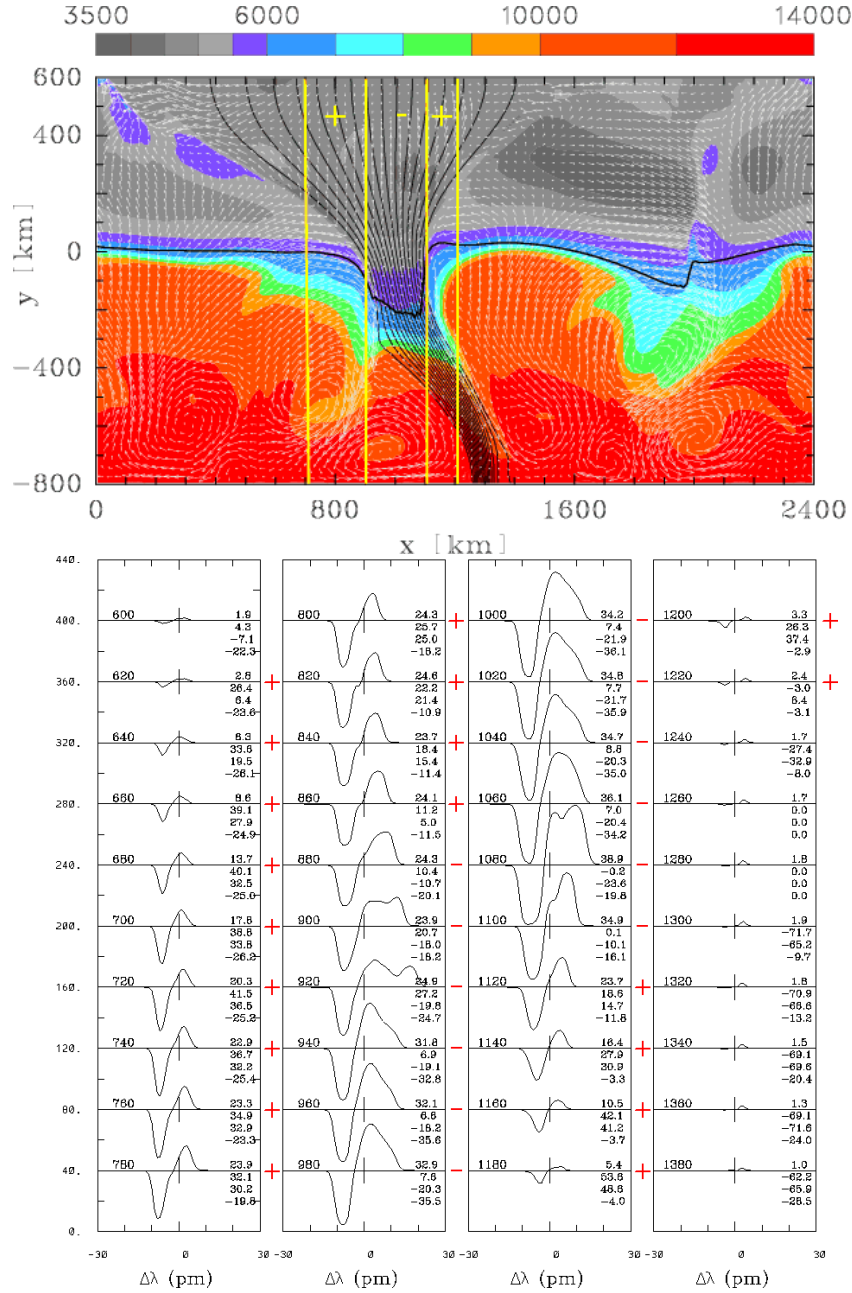


FIGURE 8. *Top:* Snapshot of a two-dimensional simulation of a magnetic flux sheet in interaction with convective motion. Color coding indicates temperature in K, white arrows the velocity. *Bottom:* Stokes V profiles that emanate from vertical lines of sight distributed over the horizontal interval between 600 and 1380 km of the simulation snapshot. Positive area asymmetries result in the two regions labeled with “+”, while the lines of sight in the middle region labeled with “-” contribute negative area asymmetries. The actual profiles emanating from each line of sight is also shown, where the mean amplitude, the amplitude asymmetry, the area asymmetry (all in %), and the zero-crossing shift in mÅ are printed (from top to bottom) on the right hand side of each panel. In addition, positive and negative area asymmetries are annotated in the right margin with a plus and a minus sign, respectively. From Steiner [40].

noting that the flux sheet is most of the time framed by a strong downflow of material [40, 21].

As mentioned in the first chapter, such a downflow is indeed visible in high resolution Dopplergrams of small-scale magnetic flux concentrations [25]. Since polarimetric measurements have not yet reached a similarly good quality in spatial resolution, the corresponding polarimetric signal of positive Stokes V area asymmetry in the periphery of flux concentrations has not yet been observationally confirmed, but I am confident that it soon will be.

Other results from the computation of synthetic Stokes profiles from three-dimensional magnetohydrodynamic simulations have recently been published by [43] and [44]. Further recent three-dimensional magnetohydrodynamic simulations of small-scale solar magnetic fields include the works [42] and [45].

THE PHYSICS OF FACULAE

With growing distance from disk center, small-scale magnetic flux concentrations grow in contrast against the quiet Sun background and become apparent as solar faculae close to the limb. Ensembles of faculae form plage and network faculae that are as conspicuous features of the white light solar disk, as are sunspots. It is therefore not surprising that they play a key role in the solar irradiance variation over a solar cycle and on shorter time scales [46, 47, 48]. Measurements of the center to limb variation of the continuum contrast of faculae are diverse, however, as the contrast is not only a function of the heliocentric angle, $\mu = \cos \theta$, but also of facular size, magnetic field strength, spatial resolution, etc., and as measurements are prone to selection effects. While many earlier measurements report a contrast maximum around $\mu \approx 0.2 \dots 0.4$ with a decline towards the limb, latest measurements [49, 50, 51, 52, 53, 54] point rather to a monotonically increasing or at most mildly decreasing contrast out to the limb.

The standard facula model [55], again consists of a magnetic flux concentration embedded in and in mechanical equilibrium with a weak-field or field-free environment as is sketched in Fig. 2. When approaching the limb, the limb side of the bright depression wall becomes ever more visible and ever more perpendicular to the line of sight, which increases its brightness compared to the limb darkened environment. At the extreme limb, obscuration by the centerward rim of the depression starts to take place, which decreases the size and possibly the contrast of the visible limb-side wall.

Recently, Lites et al. [56] and Hirzberger and Wiehr [57] have obtained excellent images of faculae with the 1 m Swedish Solar Telescope. Figure 9 (taken from [57]) shows on the left hand side network faculae at a heliocentric angle of $\mu = 0.48$ in the continuum at 587.5 nm. The solar limb is located towards the right hand side. It is clearly visible from this image that faculae are in reality partially brightened granules with an exceptionally dark and wide intergranular lane (“dark facular lane”) on the disk-center side of the contrast enhancement, which is also the location of the magnetic flux concentration. The right half of Fig. 9 shows the string of faculae within the white box of the image to the left, aligned according to the position of the dark lane. Also shown is the mean contrast profile, averaged over the alignment. Similar contrast profiles of single faculae are shown by Lites et al. [56]. Such contrast profiles pose now a new constraint

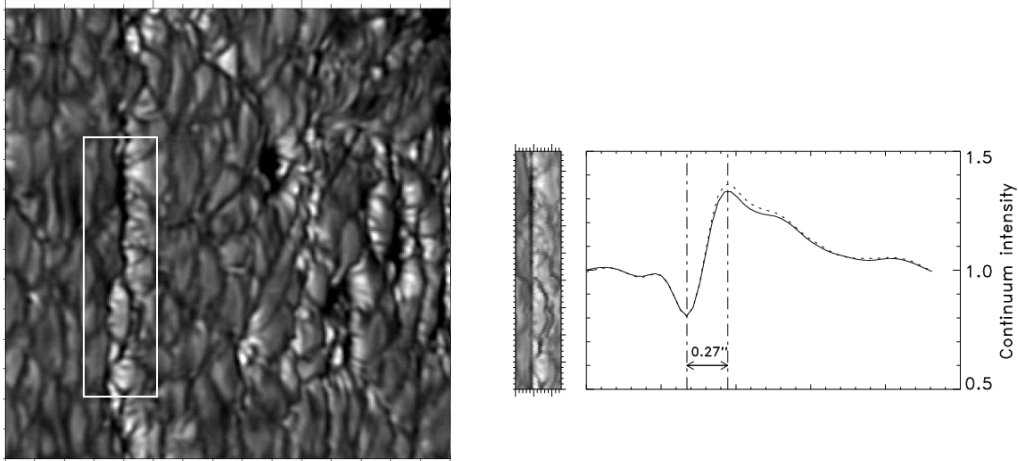


FIGURE 9. *Left:* Network faculae at a heliocentric angle of $\mu = 0.48$ in the continuum at 587.5 nm. The solar limb is to the right. *Right:* Faculae within the white box of the image to the left aligned according to the position of the dark lane, together with the mean spatial scan through the aligned faculae. The dotted curve refers to profiles for which the maximum intensity exceeds 1.3. From Hirzberger and Wiehr [57].

that any model of faculae must satisfy.

Magnetoconvective simulations as the one discussed in the previous section indeed show facular-like contrast enhancements when computing the emergent intensity along lines of sight that are inclined to the vertical direction for mimicking limb observation. Such tilted three-dimensional simulation boxes are shown in the papers by Keller et al. [58], Carlsson et al. [59], and De Pontieu et al. [60]. Keller et al. [58] also show the contrast profile of two isolated “faculae”, which however have a more symmetric shape, rather than the observed characteristic steep increase on the disk-center side with the gentle decrease towards the limb. Also they obtain a maximum contrast of 2, far exceeding the observed value of about 1.3. It is not clear what the reason for this discrepancy might be. Interestingly, the old “KGB-model” [12, 61] as well as the two-dimensional, non-stationary simulation of Steiner [62] do nicely reproduce the asymmetric shape and the dark lane.

Another conspicuous property of faculae that high-resolution images reveal is that they are not uniformly bright but show a striation not unlike to and possibly in connection with the one seen in G-band ribbons at disk center. While this feature cannot be reproduced in a two-dimensional model, it must be part of a satisfactory three-dimensional model. But so far 3-D simulations show only a rudimentary striation. This finding, rather surprisingly, indicates that the effective spatial resolution of present-day three-dimensional simulations is inferior to the spatial resolution of best current observations.

In an attempt to better understand the basic properties of faculae, Steiner [62] considers the ideal model of a magnetohydrostatic flux sheet embedded in a plane parallel standard solar atmosphere. For the construction of this model the flux-sheet atmosphere is first taken to be identical to the atmosphere of the ambient medium but shifted in the downward direction by the amount of the “Wilson depression” (the depression of the surface of continuum optical depth unity at the location of the flux concentration). The

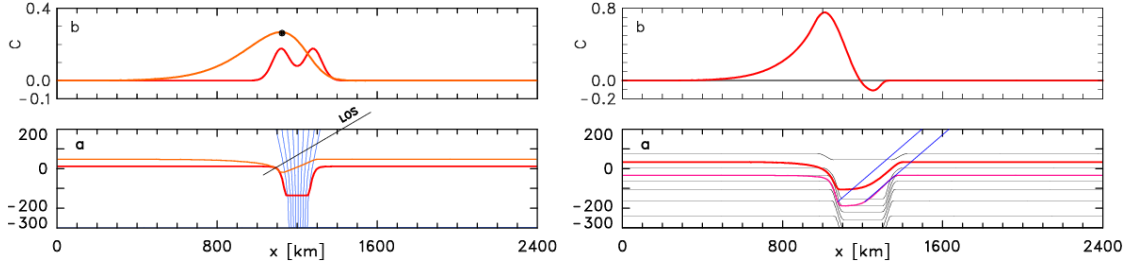


FIGURE 10. *Left:* a) Magnetic flux concentration (blue, vertically oriented lines of force, see internet version for colours) with surfaces of optical depth $\tau = 1$ for vertical lines of sight (thick/red curve) and lines of sight inclined by $\theta = 60^\circ$ to the vertical direction (thin/red curve). b) Corresponding contrast curves. All values of the light red curve left of the black dot originate from lines of sight left of the one indicated in panel a). *Right:* a) Surfaces of optical depth $\tau = 1$ and 5 (thick/red) for lines of sight inclined by 50° to the vertical, together with isotherms. b) Contrast profile. The region of negative contrast is bounded by the two oblique lines of sight indicated in panel a). Adapted from Steiner [62].

shifting results in a flux-tube atmosphere that is less dense and cooler than the ambient medium at a fixed geometrical height. In the photospheric part of the flux concentration, thermal equilibrium with the ambient medium is then enforced. Denoting with index i the flux-sheet atmosphere and with e the ambient atmosphere and with W the depth of the “Wilson depression”, we therefore have

$$T_i(z) = \begin{cases} T_e(z+W) & \text{for } \tau_c \gg 1 \\ T_e(z) & \text{for } \tau_c \ll 1, \end{cases} \quad (12)$$

where τ_c is the optical depth in the visible continuum and $\rho_i(z) < \rho_e(z) \forall z$. The lower left panel of Fig. 10 shows this configuration together with two surfaces of optical depth unity, one for vertical lines of sight (disk center), the other for lines of sight running from the top right to the bottom left under an angle of $\theta = 60^\circ$ to the vertical, like the one indicated in the figure. The upper left panel shows the corresponding continuum enhancement for disk center (double humped profile) and $\theta = 60^\circ$. Of the curve belonging to $\theta = 60^\circ$, all values left of the black dot belong to lines of sight left of the one indicated in the lower panel. This means that the contrast enhancement extends far beyond the depression proper in the limbward direction, exactly as is observed. The reason for this behaviour is explained with the help of Fig. 11 as follows.

A material parcel located in the solar atmosphere and lateral to the flux sheet “sees” a more transparent atmosphere in the direction toward the flux sheet compared to a direction under equal zenith angle but pointing away from it because of the rarefied flux-sheet atmosphere. Correspondingly, from a wide area surrounding the magnetic flux sheet or flux tube, radiation escapes more easily in the direction towards the flux sheet so that a single flux sheet/tube impacts the radiative escape in a cross-sectional area that is much wider than the magnetic field concentration proper.

The right hand side of Fig. 10 shows a similar situation as to the left but for a flux sheet that is twice as wide. The continuum contrast for lines of sight inclined by $\theta = 50^\circ$ to the vertical is shown in the top panel. It can be seen that a dark lane of negative contrast occurs on the disk-center side of the facula. It arises from the low temperature gradient of the flux-sheet atmosphere in the height range of $\tau_c = 1$ and its downshift relative to

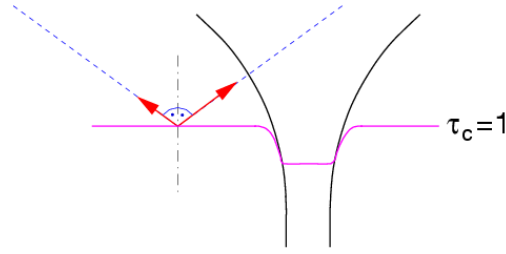


FIGURE 11. Photons preferentially escape along the line of sight to the right that traverses the magnetic flux sheet/tube in comparison to the line of sight to the left under equal zenith angle, because of the rarified (less opaque) atmosphere in the flux sheet/tube. From Steiner [14].

the external atmosphere in combination with the inclined lines of sight. One could say that the dark lane in this case is an expression of the cool “bottom” of the magnetic flux sheet.

It is remarkable that this basic, energetically not self-consistent model is capable of producing both, the facular dark lane and the asymmetrically shaped contrast curve of the facula, with realistic contrast values. The results of this basic hydrostatic model carry over to a fully self-consistent model of a magnetic flux sheet in dynamic interaction with non-stationary convective motion [62]. In this case the facular lane becomes broader and darker.

It follows from these insights that a facula is not to be identified with bright plasma that sticks, as the name may imply, like a torch out of the solar surface and as the “hillock model” of Schatten et al. [63] suggests. Rather is it the manifestation of photospheric granulation, seen across a magnetic flux concentration — granulation that appears brighter than normal in the form of so called “facular granules”. Interestingly, already Chevalier [64] wondered: “La granulation que l’on voit autour des taches plus élatante que sur les autres parties est-elle la granulation des facules ou celle de la photosphère vue à travers les facules ?” and Ten Bruggencate [65] noted that “Sie [Photosphärengranulen und Fackelgranulen] unterscheiden sich nicht durch ihre mittlere Grösse, wohl aber durch den Kontrast gegenüber der Umgebung.”

If this is true, one expects facular granules to show the same dynamic phenomena like regular granulation. Indeed, this is confirmed in a comparison of observations with three-dimensional simulations by De Pontieu et al. [60]. Fig. 12 shows on the left hand side an observed time sequence of a facula in which a dark band gradually moves from the limb side toward the disk center (down) and seemingly sweeps over and “erases” the facula temporarily. The panel on the right hand side shows the same phenomenon in a time sequence from a three-dimensional simulation. At $t = 0$ s a dark band is just above the center of the figure. It moves toward the disk center (downward in the figure), and the faculae are reduced to a weak band at $t = 90$ s.

Examination of the simulation sequence reveals that dark bands are a consequence of the evolution of granules. Often granules show a dark lane that usually introduces fragmentation of the granule. The smaller fragment often dissolves (collapses) in which case the dark lane disappears with the collapsing small fragment in the intergranular space. Exactly this process can lead to the dark band phenomenon, when a granular dark lane is swept towards the facular magnetic flux concentration. Since the facular

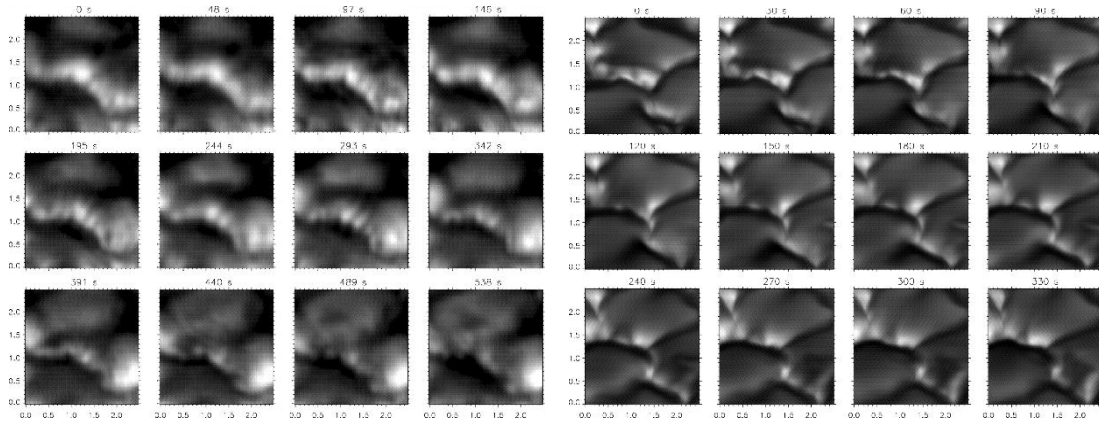


FIGURE 12. *Left*, observation: A dark band gradually moves toward the disk center (down) and seemingly sweeps over and "erases" the facula temporarily. *Right*, simulation: At $t = 0$ s a dark band is just above the center of the figure. It moves toward the disk center (downward), and the facula is reduced to a weak band at $t = 90$ s. From De Pontieu et al. [60].

brightening is seen in the disk-center facing side of granules, only granular lanes that are advected in the direction of disk center lead to facular dimming. This example nicely demonstrates how regular granular dynamics when seen across the facular magnetic field can lead to genuine facular phenomena.

Despite the major progress that we have achieved in understanding the physics of faculae over the past few years, open questions remain. These concern

- a comprehensive model of the center to limb variation of the brightness of faculae including dependence on size, magnetic flux, flux density, color, etc.,
- a quantitative agreement between simulation and observation with respect to measurements in the infrared and with respect to the observed geometrical displacement between line core and continuum filtergrams of faculae,
- the physical origin of the striation,
- a quantitative evaluation of the heat leakage caused by faculae, or
- the role of faculae in guiding magnetoacoustic waves into the chromosphere.

3-D MHD SIMULATION FROM THE CONVECTION ZONE TO THE CHROMOSPHERE

For investigating the connection between photospheric small scale magnetic fields and the chromosphere, Schaffenberger et al. [41] have extended the three-dimensional radiation hydrodynamics code CO⁵BOLD¹ to magnetohydrodynamics for studying magnetoconvective processes in a three-dimensional environment that encompasses the integral layers from the top of the convection zone to the mid chromosphere. The code is based

¹ www.astro.uu.se/~bf/co5bold_main.html

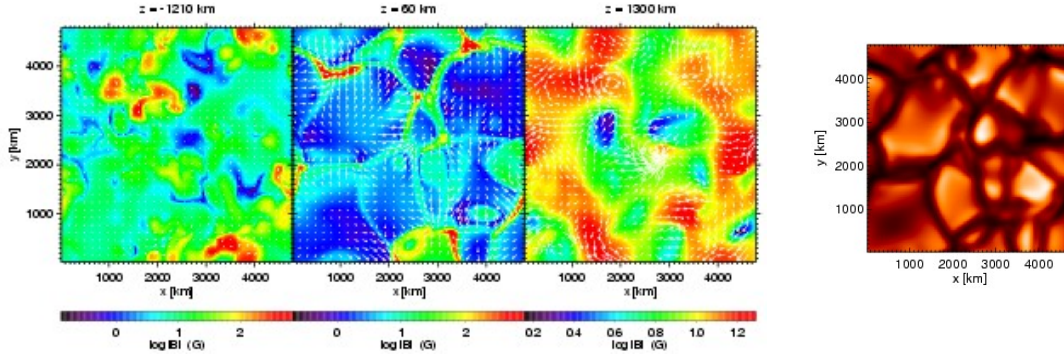


FIGURE 13. Horizontal sections through the three-dimensional computational domain. Color coding displays $\log|B|$ with individual scaling for each panel (see internet version for colours). *Left:* Bottom layer at a depth of 1210 km. *Middle:* Layer 60 km above optical depth $\tau_c = 1$. *Right:* Top, chromospheric layer in a height of 1300 km. White arrows indicate the horizontal velocity on a common scaling. Longest arrows in the panels from left to right correspond to 4.5, 8.8, and 25.2 km/s, respectively. *Rightmost:* Emergent visible continuum intensity. From Schaffenberger et al. [41].

on a finite volume scheme, where fluxes are computed with an approximate Riemann-solver [29, 30] for automatic shock capturing. For the advection of the magnetic field components, a constrained transport scheme is used.

The three-dimensional computational domain extends from 1400 km below the surface of optical depth unity to 1400 km above it and it has a horizontal dimension of 4800×4800 km. The simulation starts with a homogeneous, vertical, unipolar magnetic field of a flux density of 1 mT superposed on a previously computed, relaxed model

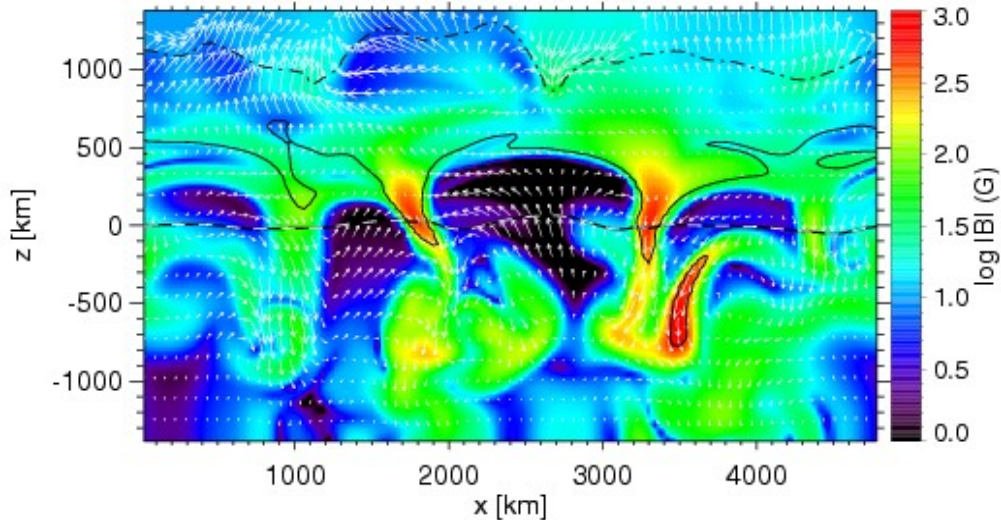


FIGURE 14. Snapshot of a vertical section through the three-dimensional computational domain, showing $\log|B|$ (color coded) and velocity vectors projected on the vertical plane (white arrows). The b/w dashed curve shows optical depth unity and the dot-dashed and solid black contours $\beta = 1$ and 100, respectively. See internet version for colours. From Schaffenberger et al. [41].

of thermal convection. This low flux density is representative for magnetoconvection in a very quiet network-cell interior. The magnetic field is constrained to have vanishing horizontal components at the top and bottom boundary, but lines of force can freely move in the horizontal direction, allowing for flux concentrations to extend right to the boundaries. Because of the top boundary being located at mid-chromospheric heights, the magnetic field is allowed to freely expand with height through the photospheric layers into the more or less homogeneous chromospheric field.

Figure 13 shows the logarithmic absolute magnetic flux density in three horizontal sections through the computational domain at a given time instant, together with the emergent Rosseland mean intensity. The magnetic field in the chromospheric part is marked by strong dynamics with a continuous rearrangement of magnetic flux on a time scale of less than 1 min, much shorter than in the photosphere or in the convection-zone layers. There, the field has a strength between 0.2 and 4 mT in the snapshot of Fig. 13, which is typical for the whole time series. Different from the surface magnetic field, it is more homogeneous and practically fills the entire space so that the magnetic filling factor in the top layer is close to unity. There seems to be no spatial correlation between chromospheric flux concentrations and the small-scale field concentrations in the photosphere.

Comparing the flux density of the panel corresponding to $z = 60$ km with the emergent intensity, one readily sees that the magnetic field is concentrated in intergranular lanes and at lane vertices. However, the field concentrations do not manifest a corresponding intensity signal like in Fig. 7 (left). This is because the magnetic flux is too weak to form a significant “Wilson depression” (as can be seen from Fig. 14) so that no radiative channeling effect (see radiative equilibrium solution in part II) takes place.

Figure 14 shows the logarithm of the absolute field strength through a vertical section of the computational domain. Overplotted are white arrows indicating the velocity field. The b/w dashed curve corresponds to the optical depth unity for vertical lines of sight. Contours of the ratio of thermal to magnetic pressure, β , for $\beta = 1$ (dot-dashed) and $\beta = 100$ (solid) are also shown. Magnetoacoustic waves that form transient filaments of stronger than average magnetic field are a ubiquitous phenomenon in the chromosphere and are also present in the snapshot of Fig. 14, e.g., along the contour of $\beta = 1$ near $x = 1200$ km and $x = 2500$ km. They form in the compression zone downstream and along propagating shock fronts. These magnetic filaments that have a field strength rarely exceeding 4 mT, rapidly move with the shock fronts and quickly form and dissolve with them. The surface of $\beta = 1$ separates the region of highly dynamic magnetic fields around and above it from the more slowly evolving field of high beta plasma below it. This surface is located at approximately 1000 km but it is corrugated and its local height strongly varies in time.

A very common phenomenon in this simulation is the formation of a ‘magnetic canopy field’ that extends in a more or less horizontal direction over expanding granules and between photospheric flux concentrations. The formation of such canopy fields proceeds by the action of the expanding flow above granule centres. This flow transports ‘shells’ of horizontal magnetic field to the upper photosphere and lower chromosphere, where shells of different field directions may be pushed close together, leading to a complicated network of current sheets in a height range from approximately 400 to 900 km.

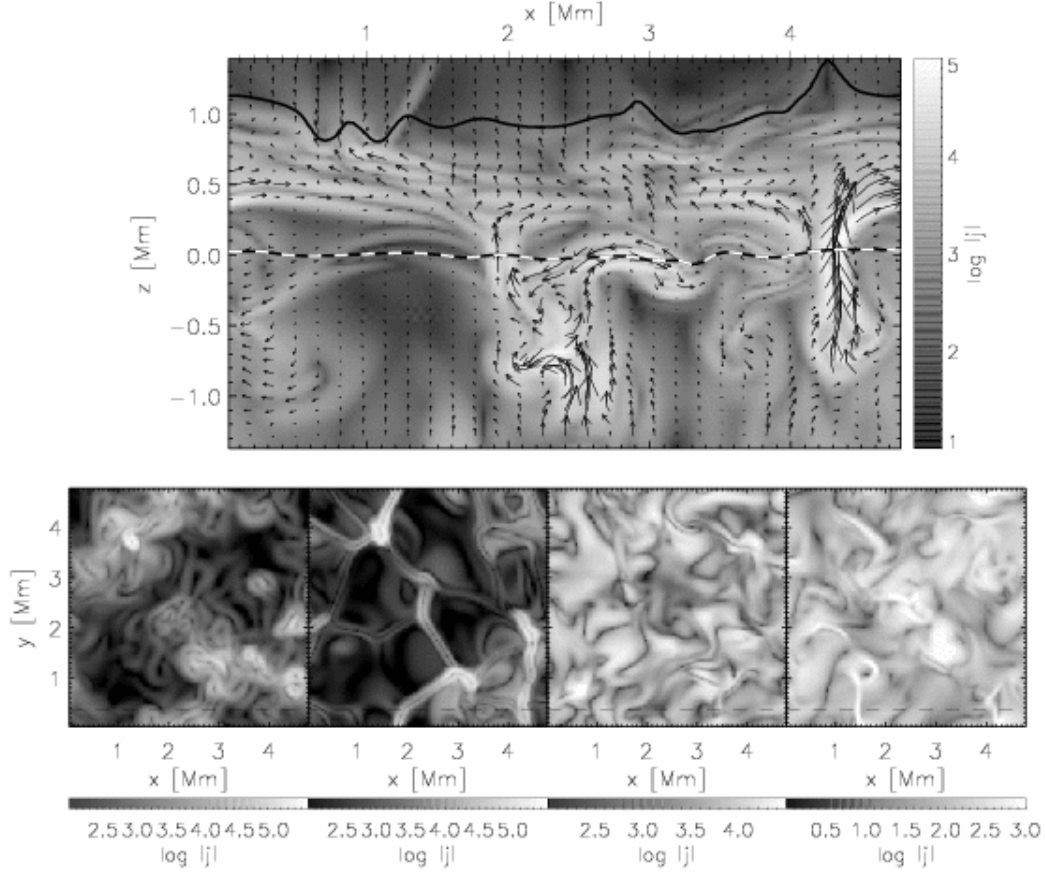


FIGURE 15. Logarithmic current density, $\log |j|$, in a vertical cross section (top panel) and in four horizontal cross sections (bottom panels) in a depth of 1180 km below, and at heights of 90 km, 610 km, and 1310 km above the mean surface of optical depth unity from left to right, respectively. The arrows in the top panel indicate the magnetic field strength and direction. The dashed line indicates the position of the vertical section. $[j] = 3 \times 10^5$ A/m². From Wedemeyer-Böhm et al. [66].

This network can be seen in Fig. 15 (top), which shows, for a typical snapshot of the simulation, the logarithmic current density, $\log |j|$, together with arrows indicating the magnetic field strength and direction. Figure 15 (bottom) shows from left to right $\log |j|$ in four horizontal cross sections in a depth of 1180 km below, and at heights of 90 km, 610 km, and 1310 km above the mean surface of optical depth unity. Higher up in the chromosphere (rightmost panel), thin current sheets form along shock fronts, e.g., in the lower left corner near $x = 1.4$ Mm.

Using molecular values for the electrical conductivity, Wedemeyer-Böhm et al. [66] derive an energy flux of 5 to 50 W m⁻² into the chromosphere caused by ohmic dissipation of these current sheets. This value is about two orders of magnitude short of being relevant for chromospheric heating. On the other hand, the employed molecular values for the conductivity might be orders of magnitude too high for to be compatible with the effective electrical conductivity of the numerical scheme determined by the inher-

ent artificial diffusion. Therefore, the ohmic heat flux might be conceivably two orders of magnitude larger than suggested by this rough estimate, so that magnetic heating by ohmic dissipation must be seriously taken into account. More advanced simulations, taking explicit ohmic diffusion into account will clarify this issue. The origin of current sheets and their microscopic nature is treated in the first chapter of the second part of these lecture notes.

FUTURE DIRECTIONS

Continuously increasing power of computational facilities together with steadily improving computational methods, expand the opportunity for numerical simulations. On the one hand, more detailed physics can be included in the simulation, on the other hand either the computational domain or the spatial and temporal resolution can be increased. In most simulations, especially when the computational domain encompasses only a small piece of a star, boundary conditions play an important role. They convey information on the outside world to the physical domain of the simulation. But this outside world is often poorly known. In order to acquire experience and intuition with respect to the influence of different types of boundary condition on the solution, one can implement and run various realizations of boundary conditions, which however also requires additional resources in computer power and time. Also the initial condition may critically determine the solution, for example the net flux and flux density of an initial, homogeneous vertical magnetic field. Boundary conditions, therefore, remain a hot topic also in future.

Most excitement in carrying out numerical simulations comes from the prospect of performing experiments with the object under investigation: experiments in the numerical laboratory. Not only that an astrophysical object can be reconstructed and simulated in the virtual world of the computational astrophysicist. Once in the computer, he has the prospect of carrying out experiments as if the celestial body was brought to the laboratory.

The following few examples shall illustrate some aspects of this.

More detailed physics

In the solar chromosphere the assumption of LTE (local thermodynamic equilibrium) is not valid. Even the assumption of statistical equilibrium in the rate equations is not valid because the relaxation time-scale for the ionization of hydrogen approaches and surpasses the hydrodynamical time scale in the chromosphere [67]. Yet, in order to take time dependent hydrogen ionization in a three-dimensional simulation into account, simplifications are needed. Leenaarts and Wedemeyer-Böhm [68] employ the method of fixed radiative rates for a hydrogen model atom with six energy levels in the three-dimensional radiation (magneto-)hydrodynamics code CO⁵BOLD. Thus, additional to

the hydrodynamic equations, they solve the time-dependent rate equations

$$\frac{\partial n_i}{\partial t} + \nabla \cdot (n_i \mathbf{v}) = \sum_{j \neq i}^{n_l} n_j P_{ji} - n_i \sum_{j \neq i}^{n_l} P_{ij}, \quad (13)$$

with P_{ij} being the sum of collisional and radiative rate coefficients, $P_{ij} = C_{ij} + R_{ij}$. The rate coefficients are now local quantities given a fixed radiation field for each transition, which is obtained from one-dimensional test calculations.

Simulations with this approach show that above the height of the classical temperature minimum, the non-equilibrium ionization degree is fairly constant over time and space at a value set by hot propagating shock waves. This is in sharp contrast to results with LTE, where the ionization degree varies by more than 20 orders of magnitude between hot gas immediately behind the shock front and cool regions further away. The addition of a hydrogen model atom provides realistic values for hydrogen ionization degree and electron density, needed for detailed radiative transfer diagnostics. Using this method, Wedemeyer-Böhm et al. [69] have computed synthetic maps of the continuum intensity at wavelengths around 1 mm for a prediction of future high resolution maps that are expected to be obtained with the Atacama Large Millimeter Array (ALMA).

Large box simulations

Benson et al. [70] have carried out first simulations with a large simulation box so as to accommodate a supergranulation cell. They started a simulation that encompasses a volume of $48 \times 48 \times 20 \text{ Mm}^3$ using 500^3 grid cells. With this simulation they hope to find out more about the large scale motions in the solar convection zone and to carry out helioseismic experiments [71, 72]. Ustyugov [45] carries out a similar calculation in a box of $(18 \text{ Mm})^3$ for which he uses $192 \times 192 \times 144$ grid points.

Hansteen [73] has carried out MHD simulations comprising a vast height range from the top layers of the convection zone into the transition region and the corona. With these simulations they seek to investigate various chromospheric features such as dynamic fibrils [74], mottles, and spicules, which are some of the most important, but also most poorly understood, phenomena of the Sun's magnetized outer atmosphere. But also the transition zone and coronal heating mechanisms are in the focus of these kinds of "holistic" simulations.

Improvements in boundary conditions

Many conventional magnetohydrodynamic simulations of the small-scale solar magnetic field assume that the horizontal component of the magnetic field vanishes at the top and bottom of the computational domain [e.g. 75, 76, 39, 41], which is a rather stark constraint, especially with respect to magnetoacoustic wave propagation and Poynting flux. Recently, Stein and Nordlund [42] have introduced an alternative condition with the possibility of advecting magnetic field across the bottom boundary (see also Fig. 6

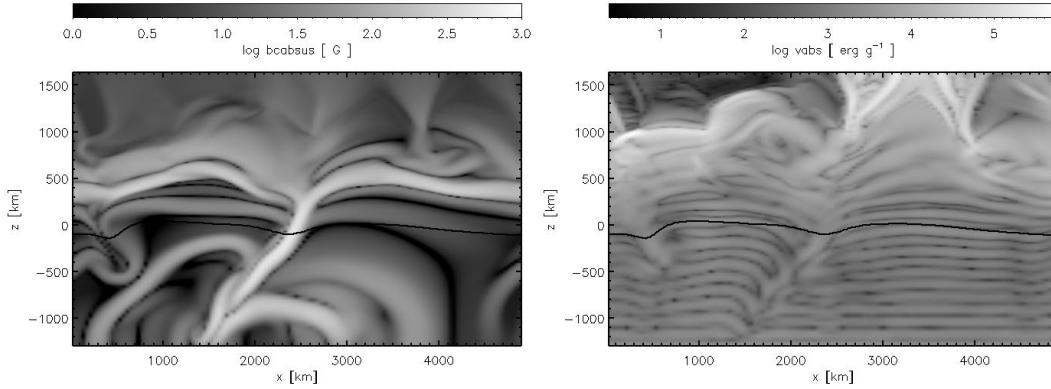


FIGURE 16. *Left:* Still image of the logarithmic magnetic flux density from a time series for the instant $t = 1368$ s after starting with an initially homogeneous vertical field of 1 mT flux density. A strong magnetic flux sheet has formed extending from $(x, z) \approx (2000, -500)$ to $(x, z) \approx (2500, 0)$. *Right:* A plane parallel wave with frequency 100 mHz travels through convecting plasma into the magnetically structured photosphere and further into the low β (magnetically dominated) chromosphere. The panel shows the difference in absolute velocity between the perturbed and the unperturbed solution 212 s after the start of the perturbation. The wave becomes strongly refracted in the low β region and at the location of the flux sheet. From Steiner [14].

right). Thus, upflows into the computational domain carry horizontal magnetic field of a prescribed flux density with them, while outflowing plasma carries whatever magnetic field it instantly has. With this condition an equilibrium in which equal amounts of magnetic flux are transported in and out of the computational domain is approached after some time. It should more faithfully model the plasma flow across the lower boundary and it allows for the effect of magnetic pumping [77, 78].

Helioseismic experiment with a magnetically structured atmosphere

With numerical experiments Steiner et al. [79] have explored the feasibility of using high frequency waves for probing the magnetic fields in the photosphere and the chromosphere of the Sun. They track an artificially excited, plane-parallel, monochromatic wave that propagates through a non-stationary, realistic atmosphere, from the convection-zone through the photosphere into the magnetically dominated chromosphere, where it gets refracted and reflected.

When comparing the wave travel time between two fixed geometrical height levels in the atmosphere (representing the formation height of two spectral lines) with the topography of the surface of equal magnetic and thermal energy density (the magnetic canopy or $\beta = 1$ surface) they find good correspondence between the two. These numerical experiments support expectations of Finsterle et al. [80] that high frequency waves bear information on the topography of the ‘magnetic canopy’. This simulation exemplifies how a piece of Sun can be made accessible to virtual experimenting by means of realistic numerical simulation.

PART II: THEORETICAL ASPECTS OF MAGNETIC FLUX TUBES

In this second part we discuss some basic properties of small-scale magnetic flux tubes. In order to do so, we abstract from the complexity and peculiarities of observed magnetic flux concentration or of simulations as the ones shown in the first part of these lecture notes. We will consider ideal flux tubes with a sharp boundary and often with a circular cross section. Although such ideal flux tubes do not exist in the non-ideal plasma of the solar photosphere, the approximation is good enough for this idealization to highlight some basic properties that also pertain to more realistic magnetic flux concentrations.

After definition of an ideal magnetic flux tube we will compute the current sheet that is associated with the tube surface and will construct a hydrostatic, vertical flux tube and study thermodynamic properties of it. We will derive a criterion for stability with respect to the interchange or fluting.

Supplementary chapters of the lectures that go beyond the scope of these notes on flows in a magnetic flux tube and how tubes of superequipartition field-strength can be formed and on wave modes supported by magnetic flux tubes can be found, e.g., in the book of Stix [81]

CONCEPT AND PROPERTIES OF MAGNETIC FLUX TUBES

A *magnetic flux tube* or *magnetic flux bundle* is defined by the surface generated by the set of field lines that intersect a simple closed curve. The magnetic flux, crossing a section S of the flux tube is given by

$$F = \int_S \mathbf{B} \cdot d\mathbf{S}. \quad (14)$$

From the divergence free nature of the magnetic field and using Gauss's law we obtain

$$\int_V \nabla \cdot \mathbf{B} dx^3 = - \overbrace{\int_{S_1} \mathbf{B} \cdot d\mathbf{s}}^{-F_1} + \overbrace{\int_{S_2} \mathbf{B} \cdot d\mathbf{s}}^{F_2} + \underbrace{\int_{\text{tube surface}} \mathbf{B} \cdot \hat{\mathbf{n}} d\sigma}_0 = 0, \quad (15)$$

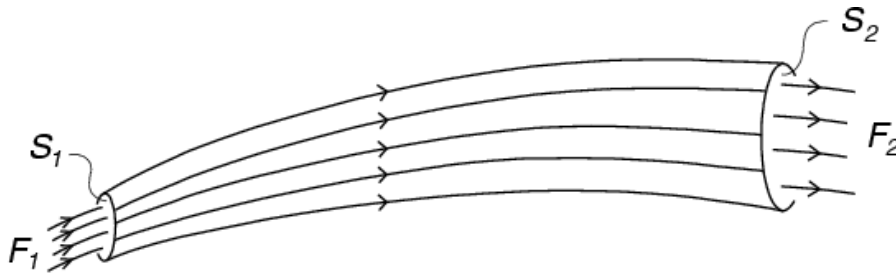


FIGURE 17. Segment of a magnetic flux tube. After Priest [82].

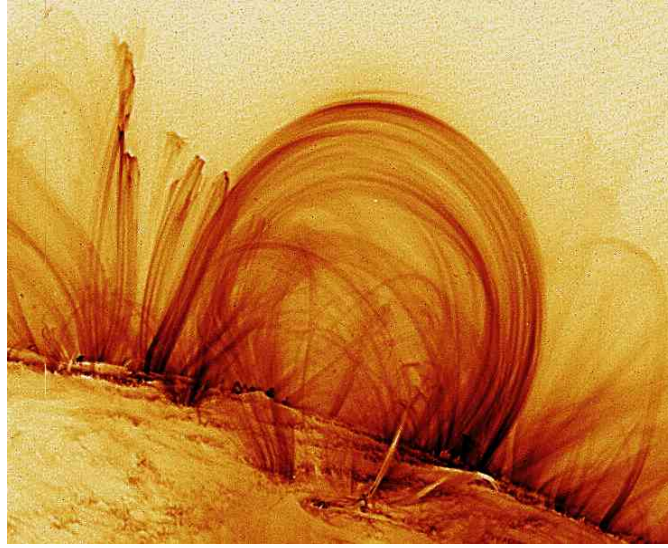


FIGURE 18. Coronal loops over the solar limb on November 6, 1999 taken in the 17.1 nm passband with the Transition Region And Coronal Explorer (TRACE). Courtesy, Stanford-Lokheed Institute for Space Research and NASA.

where we use that the flux tube surface is by definition parallel to the magnetic lines of force, hence, $\mathbf{B} \cdot \hat{\mathbf{n}} = 0$. As a consequence of $\nabla \cdot \mathbf{B} = 0$:

$$F_1 = F_2. \quad (16)$$

Hence, like a water hose that keeps mass flux constant, a magnetic flux tube conserves the magnetic flux.

Flux tubes can be considered to be the building blocks of solar magnetism. However, they must not necessarily be thought of as independent isolated structures. Coronal loops

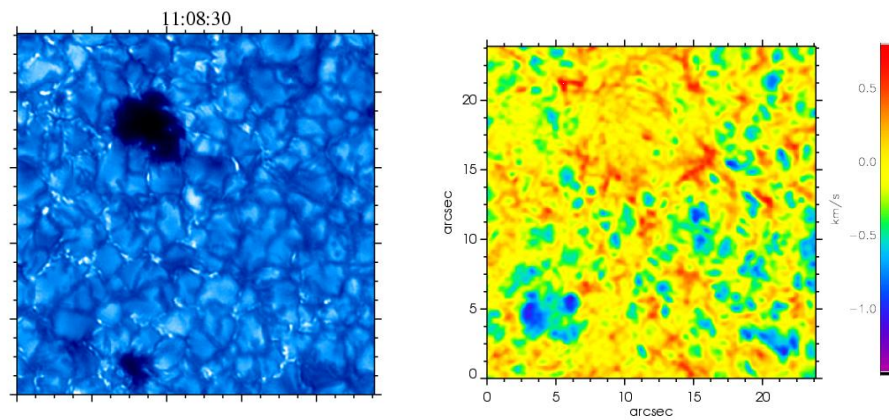


FIGURE 19. Pore (left) and corresponding Dopplergram (right). A downdraft (red) exists at the periphery of the pore. See internet version for colors. Courtesy, Kashia Mikurda, Kiepenheuer-Institut.

for example, which are close to ideal flux tubes, are embedded in an environment that may harbour magnetic fields of similar strength. They just appear like “isolated” flux tubes because the matter within it happens to be hot enough to emit radiation to become visible in certain optical passbands. Figure 18 shows examples of coronal magnetic flux tubes over the solar limb seen face-on and edge-on.

Pores are another good example of magnetic flux tubes. They often have a circular like cross section and seem to extend in close to radial direction from the convection zone into the photosphere. Unlike sunspots pores show no penumbra. Fig. 19 (left) shows a pore with granulation immediately bordering its periphery, giving the impression of an “isolated” magnetic flux tube embedded in a field-free or weak field environment. Fig. 19 (right) is the corresponding Dopplergram, showing a downdraft in the periphery of the pore very much like the downdraft indicated in Fig. 2.

Real magnetic flux tubes on the Sun are probably not ideal in the sense of Eq. (16) but are more likely “leaky” ([83]), viz., magnetic lines of force do leave and enter the tube keeping Eq. (16) only approximately conserved. Also from multidimensional simulations we know (see chapter on results from multidimensional simulations) that often field lines of a flux concentrations near the surface disperse again in shallow depths so that real flux tubes can be expected to have “open ends”. Hence, magnetic flux concentrations at the solar surface may have a flux tube character over only a short distance, typically around the level of optical depth unity.

What confines a magnetic flux tube?

In the following we take a closer look to the flux-tube surface, where a discontinuity in magnetic field strength and gas pressure exists.

Consider a magnetic flux tube, embedded in a field-free or weak-field medium. The discontinuity in magnetic field strength at the flux-tube boundary can be formally described with the step function $\theta(x)$ with $\theta(x) = 0$ for $x < 0$ and $\theta(x) = 1$ for $x > 0$. In the coordinates of the local frame given by $\hat{\mathbf{s}}$ and $\hat{\mathbf{n}}$, where $\hat{\mathbf{s}}$ is tangential to the magnetic field of the flux-tube surface (see Fig. 20), \mathbf{B} is given by $\mathbf{B} = (0, 0, B_i - [B_i - B_e]\theta(\xi))$.² Applying Ampère’s law:

$$\nabla \times \mathbf{B} = \mu \mathbf{j} \quad (17)$$

and using $\theta'(\xi) = \delta(\xi)$ (Dirac’s δ -distribution) we get:

$$\mathbf{j} = \frac{1}{\mu} (0, [B] \delta(\xi), 0), \quad (18)$$

where $[B] = B_i - B_e$. Integration over an ε -range and letting $\varepsilon \rightarrow 0$, leads to the *current sheet* which flows perpendicular to the $\hat{\mathbf{s}}\text{-}\hat{\mathbf{n}}$ plane:

$$\mathbf{j}^* = \frac{1}{\mu} [B]. \quad (19)$$

² A more refined formulation with an expansion of \mathbf{B}_i and \mathbf{B}_e around the origin of the local frame yields identical results.

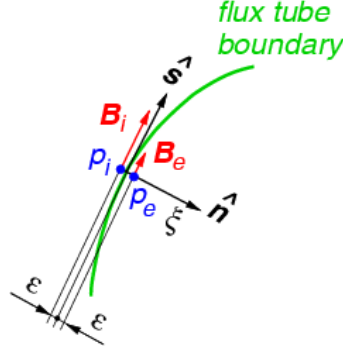


FIGURE 20. Flux-tube boundary with local coordinates. \hat{s} is tangential to a field line on the tube surface, \hat{n} perpendicular to it (main normal). The field strength at the tube surface immediately inside and outside of it are \mathbf{B}_i and \mathbf{B}_e , respectively.

Notice that this is not a regular current density since we have carried out a spatial integration in the coordinate ξ in the direction of \hat{n} across the flux-tube boundary so that \mathbf{j}^* has dimension A m^{-1} .

Thus, we have obtained as a first result that a current sheet occurs at the flux-tube surface with the current flowing perpendicular to the magnetic lines of force. Fig. 15 nicely demonstrates how current sheets may occur in the actual solar atmosphere. The characteristic double layers in the panel corresponding to 90 km above the mean surface of optical depth unity originate from the current sheet that flows on either side (surface with a sharp gradient in B) of the magnetic flux sheets that are located in the intergranular lanes.

Next, we consider the force balance starting from the momentum equation

$$\rho \frac{D\mathbf{v}}{Dt} = -\nabla p + (\mathbf{j} \times \mathbf{B}) + \rho \mathbf{g}, \quad (20)$$

where the middle term on the right hand side is the Lorentz force and \mathbf{g} the gravitational acceleration at the solar surface (optical depth $\tau_{500\text{nm}} = 1$). Again using Ampère's law, Eq. (17), we obtain for the *static case*

$$\nabla p = \frac{1}{\mu} ((\nabla \times \mathbf{B}) \times \mathbf{B}) + \rho \mathbf{g} \quad (21)$$

and further using the vector identity $(\nabla \times \mathbf{B}) \times \mathbf{B} = (\mathbf{B} \cdot \nabla) \mathbf{B} - \frac{1}{2} \nabla (\mathbf{B} \cdot \mathbf{B})$,

$$\nabla p = -\nabla \left(\frac{B^2}{2\mu} \right) + \rho \mathbf{g} + \frac{1}{\mu} (\mathbf{B} \cdot \nabla) \mathbf{B}. \quad (22)$$

Now we decompose the last term into a component parallel (\hat{s}) and perpendicular (main normal \hat{n}) to a surface field line. From $\mathbf{B} = B\hat{s}$ follows: $\mathbf{B} \cdot \nabla = B \cdot \hat{s} \cdot \nabla = B(\partial/\partial s)$ and further

$$(\mathbf{B} \cdot \nabla) \mathbf{B} = \left(B \frac{\partial}{\partial s} \right) \mathbf{B} = B \frac{\partial}{\partial s} (B\hat{s}) = B \frac{\partial B}{\partial s} \hat{s} + B^2 \frac{\partial \hat{s}}{\partial s} = \frac{\partial}{\partial s} \left(\frac{B^2}{2} \right) \hat{s} + B^2 \frac{\hat{n}}{R_c}, \quad (23)$$

where R_c is the curvature radius of the field line. Thus, we obtain:

$$\nabla p = -\nabla\left(\frac{B^2}{2\mu}\right) + \rho \mathbf{g} + \frac{\partial}{\partial s}\left(\frac{B^2}{2\mu}\right) \hat{\mathbf{s}} + \frac{B^2}{\mu} \frac{\hat{\mathbf{n}}}{R_c}, \quad (24)$$

where we note that the term $B^2/2\mu$ acts like a gas pressure, called the *magnetic pressure* [see 84, chap. 2.7]. Multiplication of this equation with $\hat{\mathbf{n}}$ yields the force balance perpendicular to the tube surface:

$$\frac{\partial p}{\partial n} = -\frac{\partial}{\partial n}\left(\frac{B^2}{2\mu}\right) + \rho \mathbf{g} \cdot \hat{\mathbf{n}} + \frac{B^2}{\mu} \frac{1}{R_c} \quad (25)$$

and integration over a small interval $[-\varepsilon, \varepsilon]$ across the tube surface gives:

$$\underbrace{\int_{p_e}^{p_i} dp}_{p_e - p_i} = - \underbrace{\int_{B_e^2/2\mu}^{B_i^2/2\mu} d\left(\frac{B^2}{2\mu}\right)}_{-\frac{1}{2\mu}(B_e^2 - B_i^2)} + \rho \mathbf{g} \cdot \hat{\mathbf{n}} 2\varepsilon + \frac{\bar{B}^2}{\mu R_c} 2\varepsilon.$$

Letting $\varepsilon \rightarrow 0$, we finally obtain:

$$p_e + \frac{B_e^2}{2\mu} = p_i + \frac{B_i^2}{2\mu}. \quad (26)$$

Thus, we have obtain as a second result that a discontinuity in pressure occurs at the flux-tube surface so that the Lorentz force is balanced by a corresponding pressure force. It is important to realize that Eq. (26) was obtained from basic principles without using the “thin flux-tube approximation”. Eq. (26) expresses that the total pressure consisting of gas pressure plus magnetic pressure is constant across the flux tube surface. This results holds generally for tangential magnetic discontinuities in a plasma. Note however, that indices i and e refer to locations in the immediate vicinity of the discontinuity.

A microscopic picture of the current sheet

It may seem surprising that an electrical current can be confined to a thin sheet in a bulk of plasma with high conductivity everywhere in space. This subsection is intended to sketch the microscopic processes that lead to this current sheet. Consider first the situation in which we have a uniformly directed magnetic field with a spatial gradient in field strength as plotted in Fig. 21 (left). The field is directed perpendicular to the drawing plane pointing out of it and increasing in strength from bottom to top. A negatively charged particle that gyrates in this field will unabatedly drift to the right because the Lorentz force, $\mathbf{F}_L = q(\mathbf{v} \times \mathbf{B})$, is not constant along the path of the particle but increases as it moves into higher field strength leading to a reduction in curvature radius. Likewise, a positively charged particle will drift to the left. Hence, electrons and

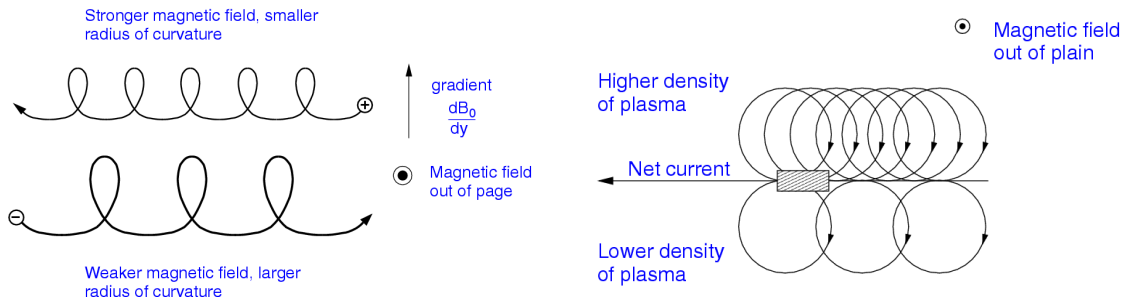


FIGURE 21. *Left:* Particle motion in a magnetic field with a transverse gradient showing grad B drift motion (adapted from Krall and Trivelpiece [85]). *Right:* Particle orbits in a plasma with a sharp density gradient resulting in a net drift current (right).

ions in a magnetic field with a transverse gradient in flux density show a *gradient B drift motion*, leading to a net electrical current.

Next we consider in Fig. 21 (right) the situation of a uniform magnetic field pointing out of the drawing plane. Instead of the gradient in field strength we have a contact discontinuity in density with a lower density in the lower half of the figure and a higher density in the upper half. In each half, positively charged particle will gyrate in a circle in the sense like indicated in Fig. 21 (right), however, there are much more gyrating particles in the upper half than in the lower half because of the difference in particle density. Considering now the hatched control volume, which straddles the contact discontinuity and which is much smaller than the gyration radius, we can readily see that much more charged particles run to the left than to the right, leading to a net positively charged current to the left and, correspondingly, a net negatively charged current to the right. Due to the imbalance of gyrating particles, an electric current results without a net transport of charges. No net current results for a control volume in either the upper or the lower half if it does not include the discontinuity.

Finally, Fig. 22 sketches the situation at the boundary of a flux tube that is thought to be embedded in a field free environment. Charged particles in the field-free plasma move on straight free paths but start to gyrate as soon as they enter the magnetic field of the flux

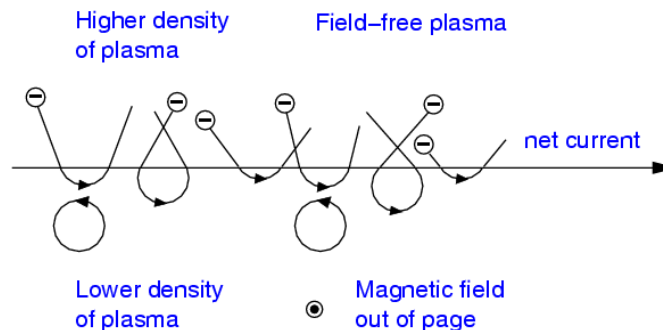


FIGURE 22. Particle orbits in a plasma with a sharp gradient in density and magnetic field strength as it occurs on the surface of a magnetic flux tube. It results a net drift current confined to the flux-tube surface.

tube, where negatively charged particles will drift to the right for the situation depicted in Fig. 22. However, this drift current will not be cancelled by gyrating particles within the flux tube because of the reduced particle number-density there. Hence, we obtain a net drift current with a net transport of charges.

THE EQUATIONS FOR A HYDROSTATIC FLUX TUBE

In this section we derive the equations that govern the magnetic structure of a vertical, axisymmetric, untwisted magnetic flux tube embedded in a gravitationally stratified, field-free atmosphere. Although such a perfectly symmetric object is an idealization that does probably not occur in reality, the basic properties of the solutions to these equations can be recovered in the more complex situations that we know from numerical simulations in a three-dimensional environment. The system of the magnetohydrostatic equations to be solved is

$$0 = -\nabla p + \rho \mathbf{g} + \mathbf{j} \times \mathbf{B}, \quad (27)$$

$$\nabla \times \mathbf{B} = \mu \mathbf{j}, \quad (28)$$

$$\nabla \cdot \mathbf{B} = 0. \quad (29)$$

We decompose Eq. (27) in components parallel and perpendicular to the magnetic field. Thus, multiplying Eq. (27) with \mathbf{B} gives

$$\mathbf{B} \cdot (\nabla p - \rho \mathbf{g}) = 0 \quad (30)$$

and taking the cross product of Eq. (27) with \mathbf{B} gives

$$\mathbf{j} = \frac{1}{B^2} \mathbf{B} \times (\nabla p - \rho \mathbf{g}), \quad (31)$$

using that $\mathbf{B} \times (\mathbf{j} \times \mathbf{B}) = B^2 \mathbf{j} - (\mathbf{B} \cdot \mathbf{j}) \mathbf{B} = B^2 \mathbf{j}$ for an untwisted axisymmetric field.

Next we reform Ampère's law, Eq. (28). Using cylindrical coordinates and Eq. (29) we first have

$$\mathbf{B} = \nabla \times \mathbf{A} = \left(\frac{1}{r} \frac{\partial A_z}{\partial \phi} - \frac{\partial A_\phi}{\partial z}, \frac{\partial A_r}{\partial z} - \frac{\partial A_z}{\partial r}, \frac{1}{r} \left(\frac{\partial}{\partial r} (r A_\phi) - \frac{\partial A_r}{\partial \phi} \right) \right), \quad (32)$$

which reduces to

$$\mathbf{B} = \left(-\frac{\partial A_\phi}{\partial z}, 0, \frac{1}{r} \frac{\partial}{\partial r} (r A_\phi) \right) \quad (33)$$

for an axisymmetric flux tube without twist. With the stream function $\Psi := r A_\phi$ we can write

$$\mathbf{B} = \left(-\frac{1}{r} \frac{\partial \Psi}{\partial z}, 0, \frac{1}{r} \frac{\partial \Psi}{\partial r} \right) \quad (34)$$

and further, taking the curl of \mathbf{B}

$$\nabla \times \mathbf{B} = \left(0, -\frac{1}{r} \frac{\partial^2 \Psi}{\partial z^2} + \frac{1}{r^2} \frac{\partial \Psi}{\partial r} - \frac{1}{r} \frac{\partial^2 \Psi}{\partial r^2}, 0 \right), \quad (35)$$

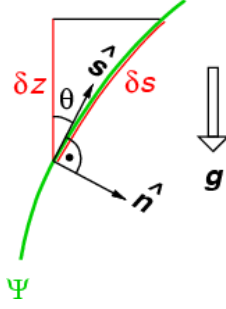


FIGURE 23. Magnetic field line Ψ with local coordinate frame. \hat{s} is tangential to the field line, \hat{n} is the main normal.

so that Ampère's law for the ϕ -component (the r - and z -components being zero), becomes (Grad-Shafranov):

$$\frac{\partial^2 \Psi}{\partial r^2} - \frac{1}{r} \frac{\partial \Psi}{\partial r} + \frac{\partial^2 \Psi}{\partial z^2} = -\mu r j_\phi. \quad (36)$$

This is a second order elliptic, inhomogeneous, partial differential equation. It is non-linear because j_ϕ depends on Ψ again as we will see further down in the text. The magnetic field components can be recovered from the stream function Ψ :

$$B_r = -\frac{1}{r} \frac{\partial \Psi}{\partial z}, \quad B_z = \frac{1}{r} \frac{\partial \Psi}{\partial r}. \quad (37)$$

Note that contours of Ψ are field lines of the system.

Now we consider Eq. (30) and Fig. 23. If gravity acts parallel to the z -axis in the negative direction and s measures the distance along a magnetic field line inclined at an angle θ to the vertical direction, we get from Eq. (30)

$$\frac{dp}{ds} + \rho g \cos \theta = 0. \quad (38)$$

Substituting the ideal gas equation for the density ρ we obtain

$$\frac{dp}{p} = -\frac{\bar{m}g}{k_B T} dz. \quad (39)$$

$H = k_B T / (\bar{m}g)$ is a length scale, called the pressure scale height, because the gas pressure drops by a factor e over this distance in the outward direction. Note that H is proportional to the temperature. \bar{m} is the mean molecular weight. Integration from a reference height $z = 0$ to an arbitrary height z along a magnetic line of force labeled with Ψ gives

$$p = p_0(\Psi) \exp \left[- \int_{\Psi,0}^{\Psi,z} \frac{dz'}{H(T(\Psi, z'))} \right]. \quad (40)$$

This equation expresses that hydrostatic equilibrium holds along magnetic field lines. Picking a field line, we obtain with this equation the gas pressure, $p(z=0)$, exerted by the mass column along this field line.

Having made use of the longitudinal component of Eq. (27) we now turn to its perpendicular component, Eq. (31). Using cylindrical coordinates $\mathbf{B} = (B_r, 0, B_z)$ and $\nabla p = (\partial p / \partial r, 0, \partial p / \partial z)$, Eq. (31) becomes

$$j_\phi = \frac{1}{B^2} \left[B_z \frac{\partial p}{\partial r} - B_r \left(\frac{\partial p}{\partial z} + \frac{p}{H} \right) \right]. \quad (41)$$

From Eq. (40) we obtain

$$\frac{\partial p}{\partial z} = -\frac{p}{H} + \frac{\partial p}{\partial \Psi} \bigg|_z \frac{\partial \Psi}{\partial z} \quad \text{and} \quad \frac{\partial p}{\partial r} = \frac{\partial p}{\partial \Psi} \bigg|_z \frac{\partial \Psi}{\partial r} \quad (42)$$

so that the above equation for j_ϕ reduces to

$$j_\phi = r \frac{\partial p}{\partial \Psi} \bigg|_z. \quad (43)$$

At the surface of the tube the magnetic field will, in general, be discontinuous, resulting in a sheet current there. Using

$$p_e - p_i = \frac{1}{2\mu} (B_i^2 - B_e^2) = \frac{1}{2\mu} (B_i - B_e)(B_i + B_e) \quad (44)$$

and Eq. (19) we finally get

$$j_\phi^* = \frac{2(p_e - p_i)}{B_i + B_e}. \quad (45)$$

The procedure for computing the magnetic structure of a vertically oriented, axisymmetric flux tube without twist is the following:

- (i) Specify an initial magnetic configuration, e.g., with the help of the thin flux-tube approximation. This initial flux tube shall be embedded in a given plane-parallel atmosphere that is thought to remain unchanged.
- (ii) Calculate the gas pressure everywhere in space using hydrostatics along magnetic lines of force, Eq. (40). Since we do not solve an energy equation here, the pressure scale height as a function of field line and height, $H(\Psi, z)$, must also be specified. An acceptable guess would be that H is independent of Ψ and identical to the scale height in the surrounding field-free atmosphere, which is approximately fulfilled if the temperature is constant in planes parallel to the solar surface. The pressure and pressure scale height in the surrounding field-free atmosphere is known from the initial, embedding atmosphere.
- (iii) Evaluate volume and current sheet using Eqs. (43) and (45). Eq. (43) applies to regions of continuous gas pressure, Eq. (45) to locations of discontinuous gas pressure and field strength like the surface of the magnetic flux tube.

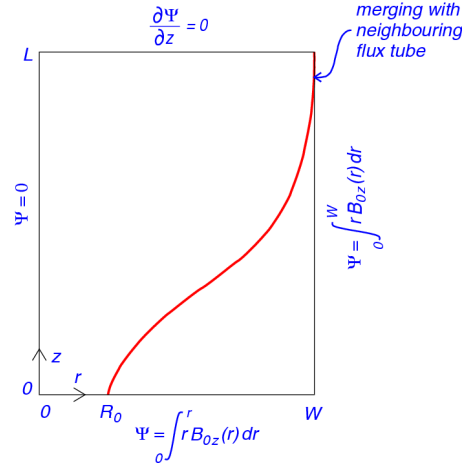


FIGURE 24. Boundary conditions for solving the elliptic partial differential equation, Eq. (36).

- (iv) Solve the Grad-Shafranov equation, Eq. (36), with appropriate boundary conditions. This leads to a new field configuration, $\Psi(r, z)$, that must not necessarily be identical to the initial magnetic configuration. Hence, one must go back to (ii) and iterate (ii) to (iv) until convergence has been achieved.

Boundary conditions need to be specified for solving Eq. (36). A plausible choice is shown in Fig. 24. The field line with $\Psi = 0$ that marks the left boundary of the computational domain coincides with the symmetry axis of the flux tube. At the bottom boundary the vertical component of the magnetic field as a function of radial distance is prescribed, which fixes $\Psi(r, z = 0)$. The boundary on the right hand side is thought to separate the flux tube from fields of neighbouring flux tubes. We can think of it as a separating field line of constant Ψ . At the top we assume that the magnetic field merges with the magnetic field of similar neighbouring flux tubes leading into a homogeneous, vertical magnetic field with vanishing horizontal component. Formally, this condition is obtained by setting $\partial\Psi/\partial z = -rB_r = 0$. The width W of the computational domain determines the filling factor f , viz., the fraction of the area at $z = 0$ that is occupied with magnetic field:

$$f = W^2/R_0^2. \quad (46)$$

Eq. (36) together with these boundary conditions constitutes a *free boundary problem* because the boundary of the magnetic flux tube is not known from the beginning but is part of the solution.

Instead of using a rectangular computational domain, Pizzo [86] uses a “body-fitted” nonorthogonal coordinate system to map the physical domain of the flux tube into a unit square computational domain. A multigrid elliptic solver is used at each iteration stage for solving the Grad-Shafranov equation. Fiedler and Cally [87] use a similar mesh in which contours of constant Ψ (field lines) constitute one coordinate, the normalized arc length along field lines the second one. Jahn [88] and Jahn and Schmidt [89] use a similar method for the construction of sunspot models.

In case of horizontal temperature equilibrium, $T_i(z) = T_e(z) = T(z)$, we have (neglecting any horizontal variation in ionization degree) $H_i(z) = H_e(z) = H(z)$. Then,

$$p_i(z) = p_{0i} \exp \left[- \int_0^z \frac{dz'}{H(T(z'))} \right] \quad p_e(z) = p_{0e} \exp \left[- \int_0^z \frac{dz'}{H(T(z'))} \right], \quad (47)$$

from which follows that $p_i(z) < p_e(z) \forall z$ assuming that p_i does not depend on radius (thin tube approximation) because $p_{0e} - p_{0i} = B_0^2/2\mu > 0$. Since $T_i(z) = T_e(z)$ it follows for the densities that $\rho_i(z) < \rho_e(z) \forall z$. Since above conditions can be expected to hold very well in the photosphere we can say that photospheric flux tubes are rarefied, one also says “partially evacuated”.

As a most simple case we explore in the following a flux tube with a constant axial field strength and gas pressure at the base level, z_0 , where the radius is R_0 . Then

$$\Psi(r, z_0) = \begin{cases} B_{z0} r^2/2 & \text{for } r \leq R_0 \\ B_{z0} R_0^2/2 & \text{for } r \geq R_0 \end{cases} \quad (48)$$

from Eq. (37) and

$$p_{i0} = p_{e0} - \frac{B_{z0}^2 + B_{r0}^2(R_0)}{2\mu} \quad (49)$$

from the requirement of pressure balance, Eq. (26). We note, that the final $B_{r0}(R_0)$ is not known from the very beginning so that the boundary condition for the pressure needs to be adjusted in the course of the iteration.

If we further assume that the temperature at a given height level is constant, then the gas pressure is constant too, so that the volume current is

$$j_\phi = r \left. \frac{\partial p}{\partial \Psi} \right|_z = 0 \quad (50)$$

and we have a potential field *inside* the flux tube. However, there remains a current sheet at the tube surface:

$$j_\phi^* = \frac{2(p_e - p_i)}{B_i + B_e}. \quad (51)$$

Fig. 25 shows the corresponding solution for a flux tube with a field strength of 0.15 T and a radius of 100 km at the base of the photosphere ($\tau_{500\text{nm}} = 1$). The figure shows representative lines of force of the magnetic field. We recall that the left hand boundary coincides with the symmetry axis of the cylindrical tube. The ring areas between two field lines contain equal amounts of magnetic flux.

Superimposed on the field-line plot are plots of the radial variation of B_r (dashed curve) and of B_z (solid curve) at different heights, both normalized to the value of B_z at the axis, indicated in gauss (10^4 T). The flux tube merges with the field of neighbouring flux tubes at a height of ≈ 500 km. The filling factor is $f = (R_0/W)^2 = 0.1$.

Due to the exponentially decreasing gas pressure in the gravitationally stratified atmosphere, the magnetic flux tube must expand with height because of pressure balance, Eq. (26), and flux conservation resulting from $\nabla \mathbf{B} = 0$. Even though, the axial field

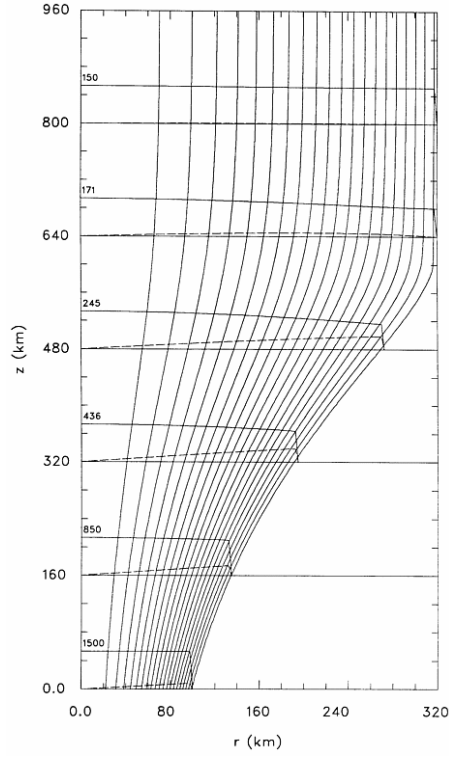


FIGURE 25. Field lines and cross sections for a cylindrically symmetric, vertical flux tube with uniform pressure and axial field strength at the base, carrying a current sheet at the surface. Superimposed on the figure are plots of the radial variation of B_r and B_z at different heights, normalized to the value of B_z at the axis, each indicated in gauss (10^4 T). Note that the vertical scale is compressed relative to the horizontal scale by a factor 1.6. From Steiner et al. [90].

strength is constant with radius at the reference height $z = 0$, this is no more the case higher up in the photosphere, where $B_z(r)$ decreases towards the flux-tube boundary. This variation of the axial field strength with flux-tube radius may become much stronger than in the case of Fig. 25 depending on the expansion rate of the flux tube, which in turn depends on the combination of internal to external atmosphere. If $H_i = H_e$ as was assumed for the flux tube of Fig. 25 it can be shown with the help of the thin flux-tube approximation that it takes about four pressure scale heights for the flux-tube radius to expand by a factor of e and about two pressure scale heights for the axial field strength to decrease by a factor of e .

Introducing the scalar function $G = rB_\phi$ one can treat the case of a twisted axisymmetric flux tube. The Grad-Shafranov equation then becomes

$$\left(\frac{\partial G}{\partial z}, \frac{\partial^2 \Psi}{\partial r^2} - \frac{1}{r} \frac{\partial \Psi}{\partial r} + \frac{\partial^2 \Psi}{\partial z^2}, -\frac{\partial G}{\partial r} \right) = -\mu r \mathbf{j}. \quad (52)$$

If $G = G(\Psi)$ (torque-free condition) we need only solve the ϕ -component, for which:

$$j_\phi = r \left. \frac{\partial p}{\partial \Psi} \right|_z + \frac{1}{\mu r} G \frac{\partial G}{\partial \Psi}. \quad (53)$$

In the absence of an external magnetic field, the magnitude of the current sheet remains the same as before: $|\mathbf{j}^*| = 2(p_e - p_i)/B_i$, directed perpendicular to the field lines at the surface and, hence, no longer purely azimuthal. The ϕ -component of the current sheet is:

$$j_\phi^* = \frac{2(p_e - p_i)}{B_i} \sqrt{1 - \left(\frac{B_\phi}{B_i}\right)^2}. \quad (54)$$

The solution procedure remains the same as before. Without even carrying out a stability analysis it can be shown that there exists an upper limit for twisting the flux tube beyond which, there is no magnetohydrostatics possible because the magnetic tension at the tube surface can no longer be counterbalanced by gas and magnetic pressure in the tube interior.

The magnetic canopy

The expansion rate of hydrostatic flux tubes critically depends on the combination of external to internal atmosphere. This is demonstrated by the following ideal model in which we assume constant but different pressure scale heights, H_e and H_i in the atmospheres external and internal to the magnetic flux tube, respectively. If $H_i > H_e$, which is equivalent to a hot flux-tube atmosphere, $T_i > T_e$, a critical height, z_{crit} , ensues, where the flux tube must strongly expand in the horizontal direction.

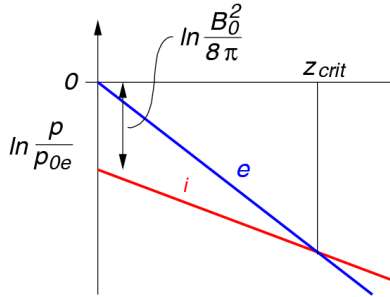


FIGURE 26. Gas pressure as a function of height within (i) and external (e) to the flux tube. At the critical height, z_{crit} , the magnetic field is forced to expand in the horizontal direction.

This situation is illustrated in Fig. 26, which shows the logarithmic gas pressure normalized to the external gas pressure at the reference height, z_0 , as a function of height in the atmosphere. Initially, the internal gas pressure, p_i , is smaller than the gas pressure in the external atmosphere, p_e , for to accommodate the magnetic flux tube with magnetic pressure $p_{\text{mag}} = p_e - p_i$. But at the critical height, z_{crit} , the internal gas pressure approaches the external gas pressure so that the magnetic field (magnetic pressure) at the tube surface must vanish, which causes the sudden horizontal expansion.

Generally, the pressure stratification in the internal and external atmosphere are given by

$$p_{i,e}(z) = p_{0i,e} \exp\left(-\int_0^z \frac{dz'}{H_{i,e}(z')}\right). \quad (55)$$

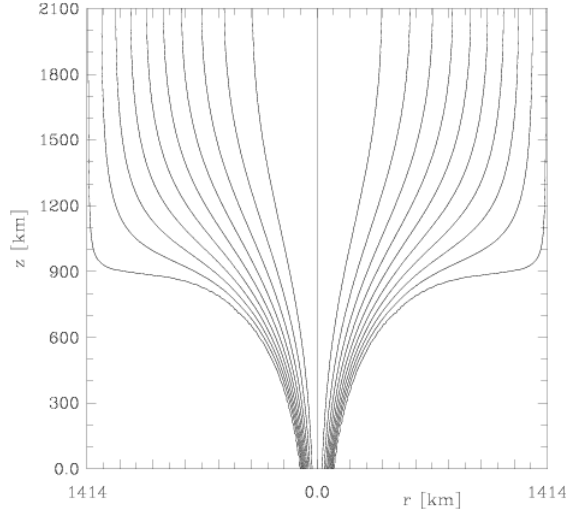


FIGURE 27. Flux tube with a standard quiet sun atmosphere embedded in a radiative equilibrium atmosphere without a chromospheric temperature rise. The field-strength at the base ($z = 0$) is 0.15 T. The field lines spread into a horizontally extending canopy field at a height of 900 km.

With $p_e(z_{\text{crit}}) = p_i(z_{\text{crit}})$ and assuming constant pressure scale heights, we obtain

$$\int_0^{z_{\text{crit}}} \left(\frac{1}{H_e} - \frac{1}{H_i} \right) dz = \ln \frac{p_{0e}}{p_{0i}} \quad \xRightarrow{H=\text{const.}} \quad z_{\text{crit}} = \frac{H_i H_e}{H_i - H_e} \ln \frac{p_{0e}}{p_{0i}} = \frac{H_i H_e}{H_i - H_e} \ln \frac{\beta_0 + 1}{\beta_0}, \quad (56)$$

where we use the plasma beta, $\beta_0 = p_{0i}/p_{\text{mag}}$, the ration of gas to magnetic pressure at the reference height z_0 .

As an example, Fig. 27 shows magnetic lines of force of a rotationally symmetric, vertical flux tube that harbours a standard quiet sun atmosphere (C' of Maltby et al. [91], Table 11). The external atmosphere is an atmosphere in radiative equilibrium showing no chromospheric temperature rise [92]. Therefore, above the temperature minimum of the internal atmosphere, at a height of approximately $z = 500$ km, it becomes distinctly cooler than the flux-tube atmosphere with the consequence that p_i rapidly approaches p_e so that the field lines spread into the horizontal direction at a height of about 900 km forming a so called *canopy field*. The strength of the canopy field is weak – in fact, the magnetic pressure must vanish at the boundary to the canopy as we have seen. Therefore, the plasma β is very inhomogeneous within a tube like that of Fig. 27 and the surface of $\beta = 1$ spreads much less dramatic with height than the peripheral field lines might suggest.

Canopy fields also occur in the superpenumbra of sunspots or in the surroundings of network magnetic fields. The latter can be directly observed in limb magnetograms of chromospheric spectral lines. This is illustrated in the sketch of Fig. 28, which shows an expanding magnetic flux tube that should be thought to represent a network magnetic flux concentration. The solar surface ($\tau_{500} = 1$) is inclined with respect to the horizontal to indicate observation near the solar limb. The hatched region is filled with magnetic field of the flux concentration, while *ff* indicates the field-free region.

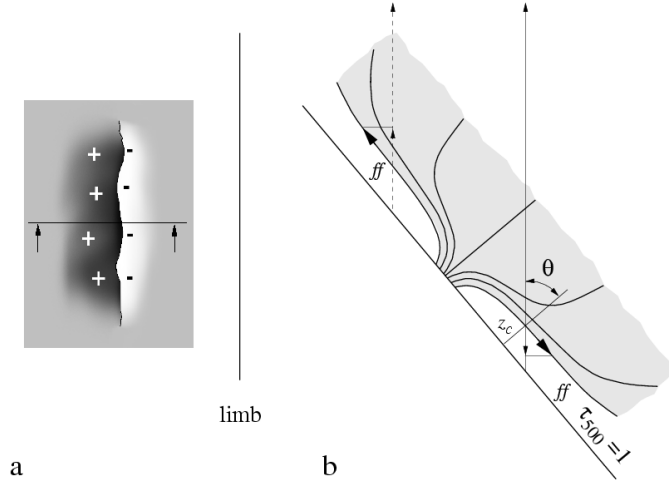


FIGURE 28. Sketch of a chromospheric magnetogram near the solar limb (a) and the corresponding magnetic configuration (b). The base of the magnetic canopy is located at a height z_c above the solar surface. From Steiner [93].

Lines of sight passing through the central network field concentration receive a magnetic field component toward the observer and so do lines of sight passing through the canopy field to the left (disk center) side of the network (dashed line of sight). The canopy field to the right (limbward) side of the network, however, gives rise to a line of sight component of opposite direction (solid line of sight). Thus, the observed magnetic polarity inverses across a line that coincides with the limbward edge of a unipolar magnetic network field as is sketched in the corresponding magnetogram to the left.

Indeed it was observed that chromospheric magnetograms of a network region that is unipolar in magnetograms of photospheric lines (that form below the canopy) show near the limb a *fringe pattern* in polarity [94]. This fringe pattern can be easily understood when we imagine the sketch of Fig. 28 (right) to be continued to a sequence of neighbouring unipolar flux concentrations, each giving rise to a chromospheric magnetogram like the one of Fig. 28 (left). From magnetograms taken in the line of Mg I b2 (517.3 nm) Jones and Giovanelli [95] derived canopy heights of 600-1000 km in quiet-Sun regions and as low as 200 km in active regions.

MAGNETIC FLUX TUBE IN RADIATIVE EQUILIBRIUM

There are two basic modes of energy transport in the solar photosphere and convection zone: radiative and convective. When in a stationary state all of the energy is transported by radiation, we have *radiative equilibrium*, conversely, in the case of pure convective transport we have *convective equilibrium*. In a stationary transport process, the frequency distribution of the radiation, or the portioning of energy between the radiative and the convective mode of transfer, may be altered; but the energy flux as a whole is rigorously conserved. Formally, this is expressed by

$$\nabla \cdot \mathbf{F}_{\text{tot}} = 0, \quad \text{where} \quad \mathbf{F}_{\text{tot}} = \mathbf{F}_{\text{rad}} + \mathbf{F}_{\text{conv}}, \quad (57)$$

assuming that no energy transport other than radiative and convective be relevant, as is usually assumed in mixing length theory.

For the two limiting cases mentioned above we have

$$\text{radiative equilibrium: } \nabla \cdot \mathbf{F}_{\text{rad}} = 0 \quad \mathbf{F}_{\text{con}} = 0, \quad (58)$$

$$\text{convective equilibrium: } \nabla \cdot \mathbf{F}_{\text{con}} = 0 \quad \mathbf{F}_{\text{rad}} = 0. \quad (59)$$

In the solar photosphere radiative energy transfer by large prevails so that $\nabla \cdot \mathbf{F}_{\text{rad}} = 0$ is a good approximation. With $I(\mathbf{r}, \hat{\mathbf{n}}, \nu)$ being the radiative intensity with frequency ν propagating in direction $\hat{\mathbf{n}}$ at location \mathbf{r} in three-dimensional space, the total radiative flux is given by

$$\mathbf{F}_{\text{rad}} = \int_{4\pi} \int_0^\infty I(\mathbf{r}, \hat{\mathbf{n}}, \nu) \hat{\mathbf{n}} d\nu d\omega. \quad (60)$$

$I(\mathbf{r}, \hat{\mathbf{n}}, \nu)$ has dimension $\text{W m}^{-2} \text{Hz}^{-1} \text{sr}^{-1}$ and correspondingly \mathbf{F}_{rad} has dimension W m^{-2} . The radiation field follows as a solution of the radiative transfer equation in three-dimensional space [96]

$$(\hat{\mathbf{n}} \cdot \nabla) I(\mathbf{r}, \hat{\mathbf{n}}, \nu) = \eta(\mathbf{r}, \nu) - \kappa(\mathbf{r}, \nu) I(\mathbf{r}, \hat{\mathbf{n}}, \nu). \quad (61)$$

The emissivity $\eta(\mathbf{r}, \nu)$ is given by $\eta(\mathbf{r}, \nu) = \kappa(\mathbf{r}, \nu) S(\mathbf{r}, \nu)$ with S being the source function. If $S(\mathbf{r})$ and $\kappa(\mathbf{r})$ are known, Eq. (61) is an ordinary first order differential equation whose solution is called the *formal solution* of the radiative transfer equation.

From these equations we obtain:

$$\nabla \cdot \mathbf{F}_{\text{rad}} = \int_{4\pi} \int_0^\infty (\hat{\mathbf{n}} \cdot \nabla) I(\mathbf{r}, \hat{\mathbf{n}}, \nu) d\nu d\omega \quad (62)$$

$$= \int_{4\pi} \int_0^\infty (\kappa(\mathbf{r}, \nu) S(\mathbf{r}, \nu) - \kappa(\mathbf{r}, \nu) I(\mathbf{r}, \hat{\mathbf{n}}, \nu)) d\nu d\omega \stackrel{!}{=} 0. \quad (63)$$

With

$$J(\mathbf{r}, \nu) = \frac{1}{4\pi} \int_{4\pi} I(\mathbf{r}, \hat{\mathbf{n}}, \nu) d\omega \quad (64)$$

being the mean intensity, we finally obtain the constraint equation for radiative equilibrium:

$$\int_0^\infty \kappa(\mathbf{r}, \nu) S(\mathbf{r}, \nu) d\nu = \int_0^\infty \kappa(\mathbf{r}, \nu) J(\mathbf{r}, \nu) d\nu. \quad (65)$$

In general we do not know the temperature distribution $T(\mathbf{r})$ that satisfies radiative equilibrium. If we start with a guess $T^{(0)}(\mathbf{r})$ for which we have calculated the correct source function $S(\mathbf{r}, \nu)$, we will find that the constraint equation for radiative equilibrium is not satisfied. It is therefore necessary to iteratively adjust $T(\mathbf{r})$ until the requirement of radiative balance is satisfied.

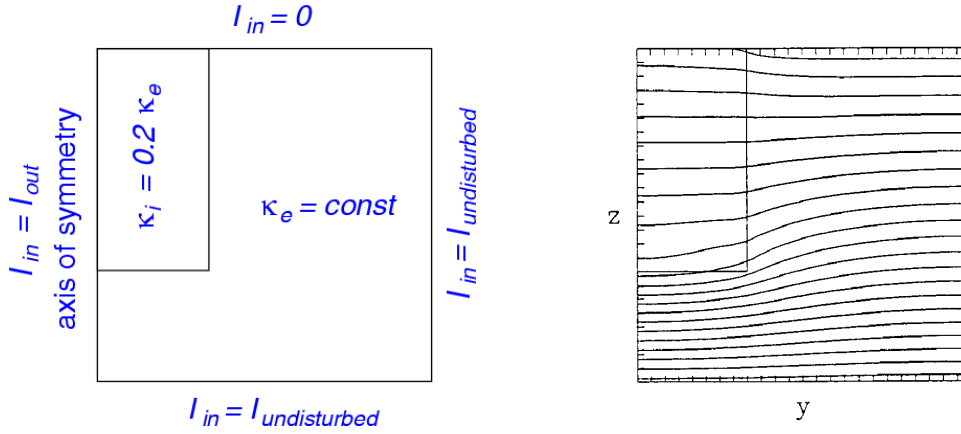


FIGURE 29. Two-dimensionally structured atmosphere in radiative equilibrium. *Left:* Radiative boundary conditions (for determining $G(\mathbf{r})$ of Eq. 66) and distribution of opacity. *Right:* Isotherms of the radiative equilibrium solution. From Steiner [97].

Assume a given temperature distribution $T(\mathbf{r})$ of the magnetohydrostatic configuration for which we also know the pressure $p(\mathbf{r})$ and density $\rho(\mathbf{r})$. This allows us to derive LTE-values for the opacities $\kappa(\mathbf{r}, \nu)$. We then are able to compute the radiation field everywhere in space \mathbf{r} and for all frequencies ν by evaluation of the formal solution of the radiative transfer equation

$$J_\nu(\mathbf{r}) = \Lambda_\nu(\mathbf{r}, \mathbf{r}') B_\nu(\mathbf{r}') + G_\nu(\mathbf{r}) , \quad (66)$$

where Λ_ν is the integral operator which adds the intensities at \mathbf{r} caused by emission at all the points \mathbf{r}' in the considered computational domain, and where G_ν is the transmitted mean intensity due to the incident radiation field into this domain. We also use strict local thermodynamic equilibrium (LTE) ($S_\nu = B_\nu$), although a scattering component could be included in the solution method that follows. Note that Λ_ν together with G_ν is just a short-hand for the integration, Eq. 64, and the formal solution of the radiative transfer equation, Eq. (61). In practice we can think of Λ_ν as a matrix operator acting on a vector of source values given at discrete spatial locations.

Defining the integral operator \mathcal{K} so that $\mathcal{K} \phi := \int_0^\infty \kappa_\nu \phi d\nu$, where ϕ is a scalar function, we can write the constraint equation for radiative equilibrium, Eq. (65), as:

$$\mathcal{K} B_\nu = \mathcal{K} \Lambda_\nu B_\nu + \mathcal{K} G_\nu . \quad (67)$$

Given an initial temperature distribution, $T^{(0)}(\mathbf{r})$, this equation is in general not satisfied. But we can compute a correction $\Delta T(\mathbf{r})$ such that

$$\mathcal{K} B_\nu(T^{(0)} + \Delta T) = \mathcal{K} \Lambda_\nu B_\nu(T^{(0)}) + \mathcal{K} G_\nu \quad (68)$$

is satisfied. Expanding $B_\nu(T + \Delta T) \approx B_\nu(T) + (\partial B_\nu / \partial T)|_T \Delta T$, we can compute the temperature correction:

$$\Delta T = \frac{\mathcal{K} (\Lambda_\nu - \mathbf{I}) B_\nu(T) + \mathcal{K} G_\nu}{\mathcal{K} (\partial B_\nu / \partial T)|_T} . \quad (69)$$

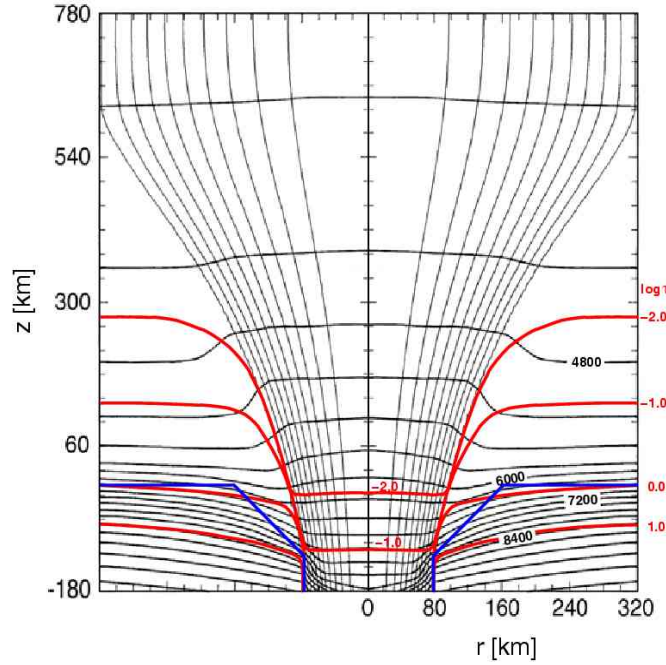


FIGURE 30. Radiative equilibrium solution for a cylindrically symmetric, vertical magnetic flux tube with a field strength of ≈ 0.15 T at $z = 0$. The horizontally running contours are isotherms labeled with the temperature in K. The curves labeled in the right margin of the figure are contours of constant optical depth for vertical lines of sight. The temperature in the convectively unstable region of the indicated pentagonal torus was prescribed. Adapted from Steiner and Stenflo [98].

For most practical purposes this iterative scheme is very slow. The next better scheme to use is a Jacobi-like iteration, in radiative transfer known as *accelerated Λ -iteration* :

$$\Delta T = \frac{\mathcal{K}(\Lambda_v - \mathbf{I})B_v(T) + \mathcal{K}G_v}{\mathcal{K}(1 - \lambda_v^*)(\partial B_v / \partial T)|_T}, \quad (70)$$

where λ_v^* is the diagonal element of the matrix representing $\Lambda_v(\mathbf{r})$. Note that $\Delta T = \Delta T(\mathbf{r})$ and that the above equation must be evaluated for each location \mathbf{r} . Since the formal solution of the transfer equation must be computed in each iteration at each location \mathbf{r} , an efficient solver is needed, which is given by the so called method of short characteristics [99, 100] and by exploiting the symmetry properties in the case of a rotationally symmetric flux tube [101].

Fig. 29 is a striking example of a two-dimensionally structured atmosphere in radiative equilibrium. The panel to the left shows the boundary condition (for determining $G(\mathbf{r})$ of Eq. 66) and the distribution of opacity. The rectangle in the upper left corner may represent a magnetic flux sheet with a rarified atmosphere and correspondingly reduced opacity. The incident radiation on the bottom and on the right side of the computational domain is computed from the undisturbed, plane-parallel atmosphere with $\kappa = \kappa_e = \text{const}$. The left side is an axis of symmetry of the configuration. The top boundary has no incident radiation. The panel to the right shows the isotherms of the radiative equilibrium solution obtained with the above given solution procedure. While in deep

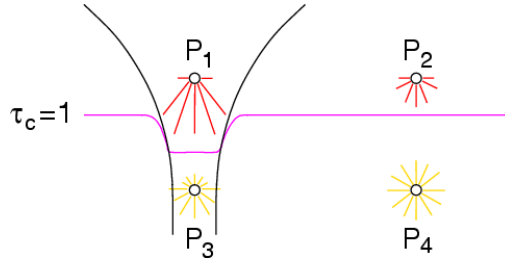


FIGURE 31. Irradiation on point P_1 located on the flux-tube axis above the level of $\tau_c = 1$ and on point P_2 located at the same geometrical height but laterally separated from the flux tube in the undisturbed atmosphere. Adapted from Steiner [17].

layers the rarified region is cooler than it is in the unperturbed surrounding atmosphere, the top layers are hotter.

This behaviour can be recovered when computing the radiative equilibrium solution of a magnetic flux tube, like the one shown in Fig. 30. It shows isotherms together with contours of constant optical depth for vertical lines of sight, labeled in the right margin of the figure. The vertically running curves represent lines of force of the magnetic field. The frequency integration in the constraint equation for radiative equilibrium, Eq. (65) was done using opacity distribution functions of Kurucz [102], thus, taking line blanketing effects into account [98]. The height scale on the left hand side originates at the optical depth $\tau_{500\text{nm}} = 1$ in the surrounding, unperturbed atmosphere, from which follows that the computational domain extends into the top surface layers of the convection zone, where the assumption of radiative equilibrium breaks down. Therefore, the temperature structure within the indicated pentagonal torus below $z = 0$ and outside the magnetic field was prescribed and kept constant when computing the radiative equilibrium solution. Resort to this stratagem obviously reveals the limits of the radiative equilibrium approach. Yet, this solution highlights a typical property of flux-tube atmospheres that can be recovered in fully self-consistent simulations: the temperature along the axis of symmetry increases in the deep photospheric layers less strong with depth than in the surrounding, unperturbed atmosphere, hence, the flux-tube atmosphere has a “flat temperature gradient”. This is a consequence of the “radiative channeling effect” by which the photospheric layers of the flux tube get heated through influx of radiation from the optically denser surroundings. This change in temperature gradient has far reaching consequences for the formation of spectral lines within the magnetic flux tube. Generally, spectral lines tend to become weaker (line weakening) with the consequence that filtergrams of spectral regions with a high density of spectral lines show magnetic elements of particularly high contrast (e.g., G-band filtergrams).

Why is the temperature in the photospheric layers of the magnetic flux tube by about 200 K higher than in the surrounding atmosphere? Consider two points P_1 and P_2 located at equal geometrical height, P_1 on the flux tube axis, P_2 far away from the flux tube in the unperturbed external atmosphere, as is illustrated in Fig. 31. P_1 receives a higher intensity of radiation from the flux tube’s hot walls (radiative channeling effect) as compared to P_2 . Both points receive equal amounts of low radiative intensity from the top. Therefore, the mean intensity is higher in P_1 than in P_2 , $J_1 > J_2$. Since in radiative

equilibrium $J = S = \int B_v dv \propto T^4$, $T_1 > T_2$. The opposite behaviour occurs for points P_3 and P_4 as long as the assumption of radiative equilibrium holds. However, the true reason for the reduced temperature in the optically thick layers of the flux tube is the inhibition of convective energy transport by the magnetic field.

INTERCHANGE INSTABILITY OF MAGNETIC FLUX TUBES

Consider a section perpendicular to the axis of a straight flux-tube as is sketched in Fig. 32. A perturbation of the flux-tube boundary in such a way that the volumes V_1 and V_2 are equal, does not change the total energy of the configuration as equal amounts of magnetic and thermal energy are exchanged. To zeroth order, the perturbation also does not change the energy state of a flux tube embedded in a stratified medium.

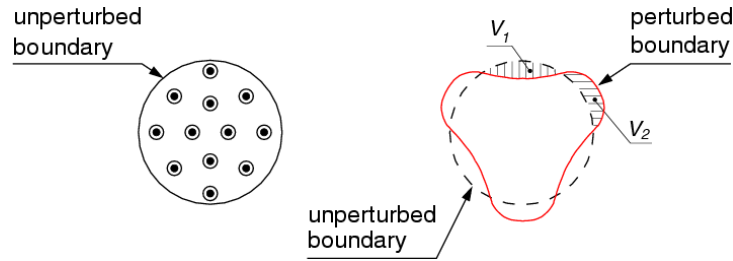


FIGURE 32. *Left:* Cross section of an unperturbed cylindrical magnetic flux tube. *Right:* Same view after perturbation showing the initial perturbation of the flutes. Adapted from Krall and Trivelpiece [85].

The instability that may evolve from this perturbation is called *interchange instability*, as the magnetic field and gas of volume 1 is interchanged with the magnetic field and gas of volume 2. It is also called *flute instability* because of the shape of the perturbed surface (like the vertical parallel grooves on a classical architectural column, called flute).

Consider a small flux-tube section with a small perturbation ξ (Fig. 33), where the grey shaded area, V_i , be the magnetic flux tube while V_e is field-free. \mathbf{n} is the surface normal pointing out of the field-free plasma. In order that there is a net restoring force on the displaced surface we must, for the indicated displacement ξ , have

$$p_{0i_{\text{tot}}} + \delta p_{i_{\text{tot}}} > p_{0e} + \delta p_e \quad \Rightarrow \quad \delta p_{i_{\text{tot}}} > \delta p_e \quad (71)$$

since for the equilibrium configuration $p_{0i_{\text{tot}}} = p_{0e}$. From this follows the condition for stability:

$$|\xi \cdot \mathbf{n}| \mathbf{n} \cdot \nabla p_e < |\xi \cdot \mathbf{n}| \mathbf{n} \cdot \nabla \left(p_i + \frac{B^2}{2\mu} \right). \quad (72)$$

This criterion also follows from a more general energy principle due to Bernstein et al. [103]. It is both, necessary and sufficient for stability.

Within the flux tube we have

$$\nabla p_i + \nabla \left(\frac{B^2}{2\mu} \right) = \rho_i \mathbf{g} + \frac{1}{\mu} (\mathbf{B} \cdot \nabla) \mathbf{B} \quad (73)$$

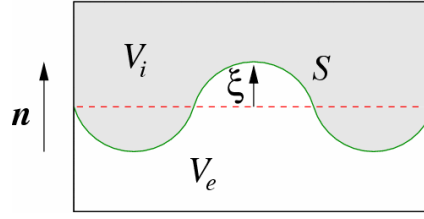


FIGURE 33. Distorted surface S displaced from the equilibrium position (dashed line). The unit vector \mathbf{n} is normal to the unperturbed surface and the section is normal to the magnetic field lines close to the tube surface. Adapted from Meyer et al. [15].

as was derived in connection with Eq. (22). In the external atmosphere we have hydrostatic equilibrium

$$\nabla p_e = \rho_e \mathbf{g} . \quad (74)$$

Using these equations in the previously derived stability criterion, Eq. (72), we obtain:

$$\mathbf{n} \cdot \left[\frac{1}{\mu} (\mathbf{B} \cdot \nabla) \mathbf{B} - (\rho_e - \rho_i) \mathbf{g} \right] > 0 . \quad (75)$$

From Eqs. (73) and (74) we have

$$\frac{1}{\mu} (\mathbf{B} \cdot \nabla) \mathbf{B} - (\rho_e - \rho_i) \mathbf{g} = \underbrace{\nabla \left(p_i + \frac{B^2}{2\mu} - p_e \right)}_{=0 \text{ on } S} , \quad (76)$$

which means that the bracketed vector in Eq. (75) is parallel to \mathbf{n} on the surface S of the flux tube.

Therefore, gravity can be eliminated taking the horizontal component of this vector. If \mathbf{h} is a horizontal vector pointing out of the flux tube into the field-free plasma we get

$$\mathbf{h} \cdot [(\mathbf{B} \cdot \nabla) \mathbf{B}] < 0 . \quad (77)$$

This means that along any field line in S the magnitude of the component of \mathbf{B} in any fixed outward horizontal direction must decrease as a function of height in the atmosphere for to have stability. For an untwisted axisymmetric flux tube this criterion can be expressed in cylinder coordinates as:

$$\left. \frac{dB_r}{dz} \right|_S < 0 . \quad (78)$$

From $\mathbf{n} \cdot (\mathbf{B} \cdot \nabla) \mathbf{B} = -\frac{B^2}{R_c}$ (see Eq. 23), where R_c is the curvature radius of the surface in axial direction, results another useful form of the stability criterion for an axisymmetric untwisted flux tube:

$$-\frac{B^2}{\mu R_c} + (\rho_e - \rho_i) g \sin \chi > 0 . \quad (79)$$

χ is the inclination of S with respect to the vertical direction.

Using a realistic model atmosphere, Meyer et al. [15] came to the conclusion that only flux tubes with magnetic flux $\Phi > 10^{11}$ Wb are stable against the flute instability. Sunspots and pores have flux in excess of 10^{11} Wb. With typical values of $R = 100$ km and $B = 0.1$ T resulting in $\Phi \approx 3 \cdot 10^9$ Wb, small-scale magnetic flux concentrations in plage and network regions are liable to the flute instability!

Indeed, from time sequences of G-band-bright-point images (e.g., [9, 10]) one gets the impression that magnetic elements are subject to fluting (see also the discussion in the first chapter of part I). On the other hand their typical life time of 6–8 minutes is still in excess of the crossing time for Alfvén or sound waves of about 100 s. Also there are bright points that undergo continual fragmentation and merging in a relatively stable location, persisting over several hours.

ACKNOWLEDGMENTS

I would like to thank the director H. M. Antia and the convener K. E. Rangarajan for having invited me to, and for their excellent organization of the 2006 Solar Physics Winter School at Kodaikanal Solar Observatory. I also thank the director of the Indian Institute of Astrophysics (IAA) S. S. Hasan for his kind hospitality during my stay at the IAA in Bangalore. This work was supported by the German Academic Exchange Service (DAAD), grant D/05/57687, and the Indian Department of Science & Technology (DST), grant DST/INT/DAAD/P146/2006.

REFERENCES

1. J. P. Mehltritter, *Solar Phys.* **38**, 43–57 (1974).
2. R. B. Dunn, and J. B. Zirker, *Solar Phys.* **33**, 281–304 (1973).
3. R. Muller, *Solar Phys.* **100**, 237 (1985).
4. R. J. Rutten, “(Inter-) Network Structure and Dynamics,” in *ASP Conf. Ser. 184: Magnetic Fields and Oscillations*, edited by B. Schmieder, A. Hofmann, and J. Staude, 1999, pp. 181–200.
5. R. J. Rutten, D. Kiselman, L. Rouppe van der Voort, and B. Plez, “Proxy Magnetometry of the Photosphere: Why are G-Band Bright Points so Bright?,” in *ASP Conf. Ser. 236: Advanced Solar Polarimetry – Theory, Observation, and Instrumentation*, edited by M. Sigwarth, 2001, pp. 445–451.
6. J. Sánchez Almeida, A. Asensio Ramos, J. Trujillo Bueno, and J. Cernicharo, *ApJ* **555**, 978–989 (2001), astro-ph/0103006.
7. S. Shelyag, M. Schüssler, S. K. Solanki, S. V. Berdyugina, and A. Vögler, *A&A* **427**, 335–343 (2004).
8. O. Steiner, P. H. Hauschildt, and J. Bruls, *A&A* **372**, L13–L16 (2001).
9. T. E. Berger, L. H. M. Rouppe van der Voort, M. G. Löfdahl, M. Carlsson, A. Fossum, V. H. Hansteen, E. Marthinussen, A. Title, and G. Scharmer, *A&A* **428**, 613–628 (2004).
10. L. H. M. Rouppe van der Voort, V. H. Hansteen, M. Carlsson, A. Fossum, E. Marthinussen, M. J. van Noort, and T. E. Berger, *A&A* **435**, 327–337 (2005).
11. W. Deinzer, G. Hensler, M. Schüssler, and E. Weisshaar, *A&A* **139**, 426–434 (1984).
12. W. Deinzer, G. Hensler, M. Schüssler, and E. Weisshaar, *A&A* **139**, 435–449 (1984).
13. C. Zwaan, *Solar Phys.* **60**, 213–240 (1978).
14. O. Steiner, “Recent progresses in the simulation of small-scale magnetic fields,” in *Modern Solar Facilities – Advanced Solar Science*, edited by F. Kneer, K. Puschmann, and A. Wittmann, 2007, pp. 321–337.

15. F. Meyer, H. U. Schmidt, and N. O. Weiss, *MNRAS* **179**, 741–761 (1977).
16. M. Schüssler, *A&A* **140**, 453–458 (1984).
17. O. Steiner, *Model calculations of solar magnetic flux tubes and radiative transfer*, Ph.D. thesis, ETH-Zürich (1990), Nr. 9292.
18. M. Bünte, O. Steiner, and V. J. Pizzo, *A&A* **268**, 299–308 (1993).
19. M. Bünte, *A&A* **276**, 236–240 (1993).
20. O. Steiner, U. Grossmann-Doerth, M. Knölker, and M. Schüssler, *ApJ* **495**, 468 (1998).
21. K. D. Leka, and O. Steiner, *ApJ* **552**, 354 (2001).
22. K. Sankarasubramanian, and T. Rimmele, *ApJ* **598**, 689–699 (2003).
23. K. Tritschler, W. Schmidt, and T. Rimmele, *Astronomische Nachrichten Supplement* **324**, 54 (2003).
24. I. Dorotović, M. Sobotka, P. N. Brandt, and G. W. Simon, *A&A* **387**, 665–671 (2002).
25. Ø. Langangen, M. Carlsson, L. R. van der Voort, and R. F. Stein, *ApJ* **655**, 615–623 (2007), astro-ph/0611741.
26. A. Nordlund, *A&A* **107**, 1–10 (1982).
27. H.-G. Ludwig, *Nichtgrauer Strahlungstransport in numerischen Simulationen stellarer Konvektion*, Ph.D. thesis, Christian-Albrechts-Universität, Kiel (1992).
28. H.-G. Ludwig, S. Jordan, and M. Steffen, *A&A* **284**, 105–117 (1994).
29. R. LeVeque, “Nonlinear Conservation Laws and Finite Volume Methods,” in *Computational Methods for Astrophysical Fluid Flow*, edited by O. Steiner, and A. Gautschi, Springer-Verlag, 1998, chap. Nonlinear Conservation Laws and Finite Volume Methods, pp. 1–159.
30. E. Toro, *Riemann Solvers and Numerical Methods for Fluid Dynamics*, Springer-Verlag, 1999.
31. R. LeVeque, *Finite Volume Methods for Hyperbolic Problems*, Cambridge University Press, 2002.
32. C. Laney, *Computational Gasdynamics*, Cambridge University Press, 1998.
33. D. S. Balsara, *ApJS* **151**, 149–184 (2004), astro-ph/0308249.
34. M. Brio, and C. Wu, *J. Comput. Phys.* **75**, 400–422 (1988).
35. S. Li, *J. Comput. Phys.* **203**, 344–357 (2004).
36. U.-L. Pen, P. Arras, and S. Wong, *ApJS* **149**, 447–455 (2003).
37. K. Powell, An approximate Riemann solver for MHD, Tech. Rep. 94-24, ICASE Langley (1994).
38. M. Wesenberg, *Efficient finite volume schemes for magnetohydrodynamic simulations in solar physics*, Ph.D. thesis, Albert-Ludwigs-Universität, Freiburg (1992).
39. A. Vögler, S. Shelyag, M. Schüssler, F. Cattaneo, T. Emonet, and T. Linde, *A&A* **429**, 335–351 (2005).
40. O. Steiner, “Flux Tube Dynamics,” in *ASP Conf. Ser. 184: Magnetic Fields and Oscillations*, edited by B. Schmieder, A. Hofmann, and J. Staude, 1999, pp. 38–54.
41. W. Schaffenberger, S. Wedemeyer-Böhm, O. Steiner, and B. Freytag, “Magnetohydrodynamic Simulation from the Convection Zone to the Chromosphere,” in *Chromospheric and Coronal Magnetic Fields*, ESA Publication SP-596, 2005, pp. 299–300.
42. R. F. Stein, and Å. Nordlund, *ApJ* **642**, 1246–1255 (2006).
43. E. V. Khomenko, S. Shelyag, S. K. Solanki, and A. Vögler, *A&A* **442**, 1059–1078 (2005).
44. S. Shelyag, M. Schuessler, S. K. Solanki, and A. Voegler, *ArXiv Astrophysics e-prints* (2007), astro-ph/0703490.
45. S. D. Ustyugov, “Three Dimensional Numerical Simulation of MHD Solar Convection on Multiprocessor Supercomputer Systems,” in *Solar MHD Theory and Observations: A High Spatial Resolution Perspective*, edited by J. Leibacher, R. F. Stein, and H. Uitenbroek, 2006, vol. 354 of *Astronomical Society of the Pacific Conference Series*, pp. 115–120.
46. M. Fligge, S. K. Solanki, and Y. C. Unruh, *A&A* **353**, 380–388 (2000).
47. T. Wenzler, S. K. Solanki, and N. A. Krivova, *A&A* **432**, 1057–1061 (2005).
48. P. Foukal, C. Fröhlich, H. Spruit, and T. M. L. Wigley, *Nature* **443**, 161–166 (2006).
49. P. Sütterlin, E. Wiehr, and G. Stellmacher, *Solar Phys.* **189**, 57–68 (1999).
50. S. Ahern, and G. A. Chapman, *Solar Phys.* **191**, 71–84 (2000).
51. A. Adjabshirizadeh, and S. Koutchmy, “Center-limb and shape-factor variations of facular elements,” in *ESA SP-506: Solar Variability: From Core to Outer Frontiers*, 2002, pp. 415–418.
52. A. Ortiz, S. K. Solanki, V. Domingo, M. Fligge, and B. Sanahuja, *A&A* **388**, 1036–1047 (2002).
53. M. Centrone, and I. Ermolli, *Memorie della Società Astronomica Italiana* **74**, 671–674 (2003).
54. F. L. Vogler, P. N. Brandt, W. Otruba, and A. Hanslmeier, “Center-to-limb variation of facular contrast derived from MLSO/RISE full disk images,” in *Solar Magnetic Phenomena*, edited by

- A. Hanselmeier, A. Veronig, and M. Messerotti, Kluwer, 2005, vol. 320 of *Astronomy and Astrophysics Space Science Library*, pp. 191–194.
55. H. C. Spruit, *Solar Phys.* **50**, 269–295 (1976).
 56. B. W. Lites, G. B. Scharmer, T. E. Berger, and A. M. Title, *Solar Phys.* **221**, 65–84 (2004).
 57. J. Hirzberger, and E. Wiehr, *A&A* **438**, 1059–1065 (2005).
 58. C. U. Keller, M. Schüssler, A. Vögler, and V. Zakharov, *ApJ* **607**, L59–L62 (2004).
 59. M. Carlsson, R. F. Stein, Å. Nordlund, and G. B. Scharmer, *ApJ* **610**, L137–L140 (2004).
 60. B. De Pontieu, M. Carlsson, R. Stein, L. Rouppe van der Voort, M. Löfdahl, M. van Noort, Å. Nordlund, and G. Scharmer, *ApJ* **646**, 1405–1420 (2006).
 61. M. Knölker, and M. Schüssler, *A&A* **202**, 275–283 (1988).
 62. O. Steiner, *A&A* **430**, 691–700 (2005).
 63. K. H. Schatten, H. G. Mayr, K. Omidvar, and E. Maier, *ApJ* **311**, 460–473 (1986).
 64. S. Chevalier, *Ann. de l’Obs. de Zô-sè* **8**, C1 (1912).
 65. P. Ten Bruggencate, *ZAp* **19**, 59–67 (1940).
 66. S. Wedemeyer-Böhm, O. Steiner, J. Bruls, and W. Rammacher, “What is heating the quiet-Sun chromosphere?,” in *Coimbra Solar Physics Meeting on The Physics of Chromospheric Plasmas*, edited by P. Heinzel, I. Dorotovič, and R. Rutten, ASP Conference Series, 2007, pp. 193–202, astro-ph/0612627.
 67. F. Kneer, *A&A* **87**, 229–235 (1980).
 68. J. Leenaarts, and S. Wedemeyer-Böhm, *A&A* **460**, 301–307 (2006), astro-ph/0608620.
 69. S. Wedemeyer-Böhm, H.-G. Ludwig, M. Steffen, and B. Freytag, *A&A* (2007), submitted.
 70. D. Benson, R. Stein, and Å. Nordlund, “Supergranulation Scale Convection Simulations,” in *ASP Conf. Ser. 354: Solar MHD Theory and Observations: A High Spatial Resolution Perspective*, edited by J. Leibacher, R. F. Stein, and H. Uitenbroek, 2006, pp. 92–96.
 71. D. Georgobiani, J. Zhao, A. G. Kosovichev, D. Benson, R. F. Stein, and Å. Nordlund, *ApJ* **657**, 1157–1161 (2007), astro-ph/0608204.
 72. J. Zhao, D. Georgobiani, A. G. Kosovichev, D. Benson, R. F. Stein, and Å. Nordlund, *ApJ* p. in press (2007), astro-ph/0612551.
 73. V. H. Hansteen, “Initial simulations spanning the upper convection zone to the corona,” in *IAU Symposium*, edited by A. V. Stepanov, E. E. Benevolenskaya, and A. G. Kosovichev, 2004, pp. 385–386.
 74. V. H. Hansteen, B. De Pontieu, L. Rouppe van der Voort, M. van Noort, and M. Carlsson, *ApJ* **647**, L73–L76 (2006), astro-ph/0607332.
 75. N. O. Weiss, D. P. Brownjohn, P. C. Matthews, and M. R. E. Proctor, *MNRAS* **283**, 1153–1164 (1996).
 76. F. Cattaneo, T. Emonet, and N. Weiss, *ApJ* **588**, 1183–1198 (2003).
 77. S. Tobias, N. Brummell, T. Clune, and J. Toomre, *ApJ* **502**, 177 (1998).
 78. M. Ossendrijver, M. Stix, A. Brandenburg, and G. Rüdiger, *A&A* **394**, 735–745 (2002), astro-ph/0202299.
 79. O. Steiner, G. Vigeesh, L. Krieger, S. Wedemeyer-Böhm, W. Schaffenberger, and B. Freytag, *Astron. Nachr./AN* **328**, 323–328 (2007), astro-ph/0701029.
 80. W. Finsterle, S. Jefferies, A. Cacciani, P. Rapex, and S. McIntosh, *ApJ* **613**, L185–L188 (2004).
 81. M. Stix, *The Sun*, Springer, Berlin, 2002.
 82. E. R. Priest, “Magnetohydrodynamics,” in *Plasma Astrophysics*, edited by A. O. Benz, and T. J.-L. Courvoisier, Springer-Verlag, 1994, pp. 1–109.
 83. F. Cattaneo, N. H. Brummell, and K. S. Cline, *MNRAS* **365**, 727–734 (2006).
 84. E. Priest, *Solar Magnetohydrodynamics*, D. Reidel, Dordrecht, 1982.
 85. N. Krall, and A. Trivelpiece, *Principles of Plasma Physics*, McGraw-Hill Company, New York, 1973.
 86. V. J. Pizzo, *ApJ* **365**, 764–777 (1990).
 87. R. A. S. Fiedler, and P. S. Cally, *Solar Phys.* **126**, 69–88 (1990).
 88. K. Jahn, *A&A* **222**, 264–292 (1989).
 89. K. Jahn, and H. U. Schmidt, *A&A* **290**, 295–317 (1994), astro-ph/9410011.
 90. O. Steiner, G. W. Pneuman, and J. O. Stenflo, *A&A* **170**, 126–137 (1986).
 91. P. Maltby, E. H. Avrett, M. Carlsson, O. Kjeldseth-Moe, R. L. Kurucz, and R. Loeser, *ApJ* **306**, 284–303 (1986).

92. L. S. Anderson, *ApJ* **339**, 558–578 (1989).
93. O. Steiner, “Chromosphere: Magnetic canopy,” in *Encyclopedia of Astronomy and Astrophysics*, edited by P. Murdin, Nature Publishing Group, Macmillan Publishers Ltd., UK, www.ency-astro.com, 2000.
94. R. G. Giovanelli, *Solar Phys.* **68**, 49–69 (1980).
95. H. P. Jones, and R. G. Giovanelli, *Solar Phys.* **79**, 247–266 (1982).
96. D. Mihalas, *Stellar Atmospheres*, W. H Freeman and Company, San Francisco, 1978.
97. O. Steiner, *A&A* **231**, 278–288 (1990).
98. O. Steiner, and J. O. Stenflo, “Model Calculations of the Photospheric Layers of Solar Magnetic Fluxtubes,” in *IAU Symposium*, edited by J. O. Stenflo, 1990, pp. 181–184.
99. P. Kunasz, and L. Auer, *J.Q.S.R.T.* **39**, 67–79 (1988).
100. P. Kunasz, and L. Olson, *J.Q.S.R.T.* **39**, 1–12 (1988).
101. O. Steiner, A short description of CYL2D, a radiative transfer code, Tech. rep., Kiepenheuer-Institut (1993), <http://www.kis.uni-freiburg.de/~steiner/cyl2d.ps.gz>.
102. R. L. Kurucz, *ApJS* **40**, 1–340 (1979).
103. I. B. Bernstein, E. A. Frieman, M. D. Kruskal, and R. Kulsrud, *Proc. R. Soc. London A* **244**, 17–40 (1958).